Sandwich structures with repairable cores based on truncated cube cells

Hedayati, Reza; Yousefi, Armin; Bodaghi, Mahdi

DOI
10.1016/j.compositesb.2022.110124

Publication date
2022

Document Version
Final published version

Published in
Composites Part B: Engineering

Citation (APA)
Hedayati, R., Yousefi, A., & Bodaghi, M. (2022). Sandwich structures with repairable cores based on truncated cube cells. *Composites Part B: Engineering*, *243*, Article 110124. https://doi.org/10.1016/j.compositesb.2022.110124

Composites Part B 243 (2022) 110124

Contents lists available at ScienceDirect

Composites Part B

journal homepage: www.elsevier.com/locate/compositesb

Sandwich structures with repairable cores based on truncated cube cells

Reza Hedayati [a,**], Armin Yousefi [b], Mahdi Bodaghi [b,*]

[a] Department of Aerospace Structures and Materials (ASM), Faculty of Aerospace Engineering, Delft University of Technology, 2600 AA, Delft, the Netherlands
[b] Department of Engineering, School of Science and Technology, Nottingham Trent University, Nottingham, NG11 8NS, UK

ARTICLE INFO

Keywords:
3D printing
Truncated cube
Sandwich structures
FEM
Analytical solution
Repairable cores

ABSTRACT

With dramatic increase in 3D printing applications in industry, sandwich panels with 3D printed cores have gained a lot of attention recently. In harmony with global movement towards sustainability and low-carbon emission industries, sandwich panels with easy-to-repair and cost-effective cores would be very attractive structures. In this regard, implementing separated cells for constructing lattice structures instead of using back-to-back lattice structures makes repairing local damages in the core easier and more cost-effective. Ideally, a damaged cell can be replaced with an intact new cell without the need to change the whole core structure. In this study, mechanical responses of a single truncated cube unit cell, a well-known geometry for constructing regular lattices has been studied analytically, numerically, and experimentally. Analytical relationships were derived for stiffness, yield stress, and Poisson's ratio of a single unit cell. Samples were 3D printed and tested mechanically in large deformation regime. A good agreement between results from analytical derivations, numerical simulations, and experiments was observed. It was shown that an equilateral truncated cube structure has a yield stress at least twice of that for a simple cube structure. Three types of repairable sandwich panels with different uniform core densities as well as four graded cores were studied as well. The functionally graded sandwich panels presented the best performance while considering both energy absorption capacity and mass. The best functionally graded sandwich panels (Type 4) showed an increase in specific energy absorption (SEA) by almost 21% and a decrease in maximum displacement by 2.5% with respect to the second-ranking best option.

1. Introduction

Nowadays, aerospace, marine, and automobile industries extensively take advantage of optimal properties of sandwich structures, including lightness, high impact resistance (excellent energy absorption capability), and high bending stiffness over conventional fully-metallic structures. As a particular type of sandwich structure, sandwich panels consist of three main components: face sheets, central core, and bonding (adhesive layers) between the face sheets and the core [1–7]. The high energy absorption capability of sandwich panels makes these structures even more interesting for industrial applications [8–11]. With dramatic increase in 3D printing applications, fully 3D printed sandwich panels or conventional sandwich panels with 3D printed cores have earned a lot of attention recently [12–15].

Additive manufacturing (AM) techniques such as selective laser melting (SLM) [16], selective electron beam melting (SEBM) [17], Multijet fusion (MJF) [18], and direct metal laser sintering (DMLS) deliver tailor-made 3d-printed structures. The high-quality, low-cost, and fast production procedures available by 3D printing technologies are very advantageous for numerous applications, including tailor-made sandwich structures. 3D printing technologies offer the possibility of manufacturing lattice structures with pre-designed micro-architectures.

Different types of repeating unit cells have been proposed for constructing lattice structures. Cube [19], rhombic dodecahedron [19,20], diamond [19,21], truncated octahedron (also known as Kelvin foam) [19,20,22], square horseshoe [15], and Voronoi [20,22] structures are the most studied morphologies using finite element method (FEM). Other micro-lattice structures such as body-centered cubic structure (BCC) [23,24], body-centered cubic structure with vertical pillars (BCC-Z) [23], facet-centered cubic structure with vertical pillars (F2FCC-Z) [25,26], hexagonal [27,28], octahedral [29], 3D-Kagome [30,31], and pyramidal [30] geometries have also been investigated by different researchers. As one of the first works, Ashby and Gibson [32] obtained analytical relationships for elastic and plastic response of simple cubic structure. More recently, analytical solutions have also been presented for diamond [33], rhombic dodecahedron [34,35],

* Corresponding author.
** Corresponding author.
E-mail addresses: r.hedayati@tudelft.nl (R. Hedayati), mahdi.bodaghi@ntu.ac.uk (M. Bodaghi).

https://doi.org/10.1016/j.compositesb.2022.110124
Received 28 April 2022; Received in revised form 21 June 2022; Accepted 7 July 2022
Available online 15 July 2022

rhombicuboctahedron [36], 2D and 3D auxetic re-entrant [37,38], and truncated octahedron [39] geometries.

In our previous study [40], the mechanical response of lattice structures assembled from different types of unit cells were compared to each other. The results showed that at the same relative density, the structures based on cube and truncated cube unit cells have the highest levels of yield stress. They were also among the unit cells with the highest elastic modulus. The noted high relative yield stress and elastic modulus provides the opportunity of constructing structures with favourable levels of yield stress and elastic modulus. If one needs structures with lower elastic modulus/yield stress, they can simply decrease the relative density to the level which gives the required mechanical properties. Among the two noted topologies, the cubic structure has the drawback of being very susceptible to buckling. Therefore, in this study, truncated cube geometry was selected for filling the core of the sandwich structure.

The majority of the previous analytical solutions are obtained for unit cells located in a lattice structure where neighboring unit cells are in touch with each other (in the rest of the paper, denoted as *back-to-back* lattice structures). An interesting and useful type of lattice structure would be the case where the neighboring unit cells are not in direct contact with each other (in the rest of the paper, denoted as *separated* lattice structures). Such lattice structures, while preserving some useful aspects of the back-to-back lattice structures, can provide some additional advantages such as easy repairability. Therefore, studying their behavior in elastic and post-elastic regimes are very beneficial. Although analytical solutions for truncated cube in the back-to-back lattice structures have been derived previously [41], no analytical solutions have yet been obtained for a single truncated cube structure.

Truncated cube has not been extensively studied numerically or experimentally. Crushing behavior of closed-cell foams with truncated cube morphology, as a good representative of traditional foams, has been investigated numerically by a number of researchers such as [42–46]. Elastic modulus, Poisson's ratio and yield stress of open- and closed-cell truncated cube periodic lattices has also been investigated numerically by Vigliotti and Pasini [44].

As explained earlier, the relationships and results obtained in this paper for a single unit cell would be useful to investigate the mechanical response of unit cells employed as a core for sandwich panels. Sandwich panels having a core consisting of separated unit cells would be very beneficial for sustainable applications where easy repair of local failures of the core is highly needed. In this regard, a damaged cell can be replaced by a new cell without the need to change the whole core. This particular application will be investigated comprehensively in this study. In addition, sandwich structures with functionally graded cores where the core structure's geometry varies spatially are more effective regarding energy absorption and weight reduction [47,48].

The main aim of the current study is to design sandwich panels with high energy absorption capability and low mass by employing truncated unit cells which provide a unique possibility for repairability of the cells. Different steps of the present study, from unit cell design to unit cell testing, sandwich panel design and sandwich panel application are depicted in Fig. 1.

In this study, first the elastic mechanical properties of truncated cube unit cell are studied by developing numerical and analytical solutions with experimental validation. Analytical relationships are derived for stiffness, yield stress, and Poisson's ratio of a single unit cell having three different cross-section types, namely circle, square, and equilateral triangle. The obtained formulas are compared to numerical results to evaluate the validity of the relationships. For the analytical calculations, Euler-Bernoulli beam theory is employed. The finite element solver uses Timoshenko beam theory for relating the force and displacement in each strut. All the relationships are stated as functions of parameter α (which will be defined in the next section). By assigning different values to α, the obtained formulas are applicable to cubes with different levels of truncations, including a cube and an octahedron at extreme values of α. The mechanical behavior of unit cells in the large deformation regime are validated by mechanical testing of 3D printed samples. As the next step, the truncated unit cells are used as repairable building blocks for the core of sandwich panels. The energy absorption capability considering the weight of sandwich panels are studies numerically. Moreover, novel, effective, functionally graded sandwich structures are designed and compared with sandwich structures with uniform core densities.

2. Materials and methods

2.1. Apparent density

Each unit cell consists of 24 inclined edges with length l (each shared by another adjacent unit cell) and 12 uninclined edges with length $m = \alpha l$ (each also shared by three adjacent unit cells), see Fig. 2d where dimensions m and l are marked. Each truncated cube unit cell with cell

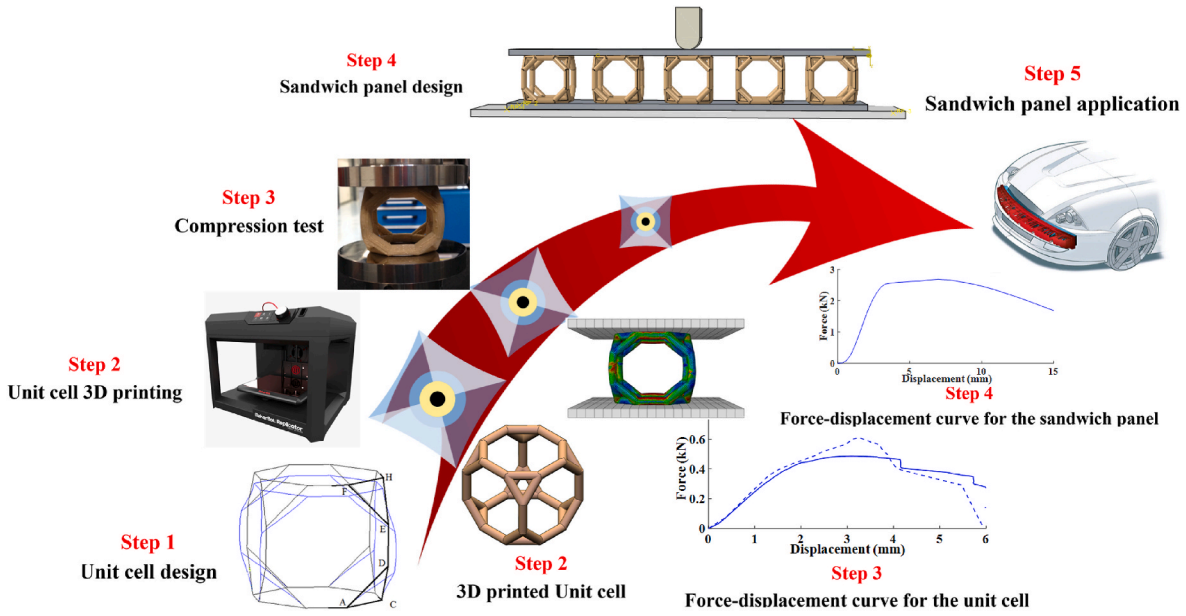

Fig. 1. Steps of designing sandwich panels with repairable cores.

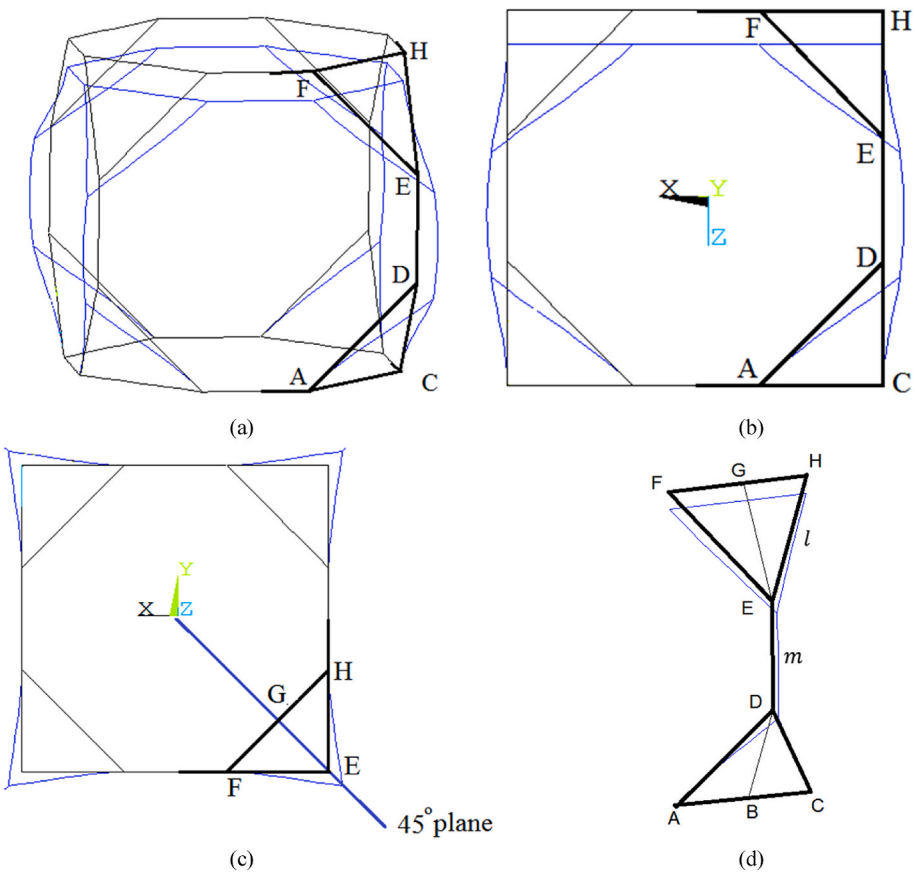

Fig. 2. A truncated cube unit cell before and after deformation under compressive loading: (a) 3D view, (b) frontal 2D view, (c) top 2D view, and (d) deformation of ¼ of a unit cell. The thin black and thin blue lines represent the geometry of the unit cell before and after deformation, respectively. The thick black lines demonstrate ¼ of the unit cell considered for analytical study. (For interpretation of the references to colour in this figure legend, the reader is referred to the Web version of this article.)

dimension a occupies a volume of $(\sqrt{2}l+m)^3 = (\alpha+\sqrt{2})^3 l^3$. Therefore, the apparent density of the structure can be found by

$$\mu=\frac{mass}{V}=\frac{\frac{24}{2}\{\pi r^2 l\}+\frac{12}{4}\{\pi r^2 \alpha l\}}{(\alpha+\sqrt{2})^3 l^3}=\frac{\pi(12+3\alpha)}{(\alpha+\sqrt{2})^3}\left(\frac{r}{l}\right)^2 \tag{1}$$

For $\alpha = 1$, the apparent density becomes:

$$\mu=\frac{m}{V}=\frac{15\pi}{(1+\sqrt{2})^3}\left(\frac{r}{l}\right)^2 \tag{2}$$

For the square cross-section with cross-section side length of b, we have:

$$\mu=\frac{m}{V}=\frac{\frac{24}{2}\{b^2 l\}+\frac{12}{4}\{b^2\alpha l\}}{(\alpha+\sqrt{2})^3 l^3}=\frac{12+3\alpha}{(\alpha+\sqrt{2})^3}\left(\frac{b}{l}\right)^2 \Rightarrow \mu=\frac{15}{(1+\sqrt{2})^3}\left(\frac{b}{l}\right)^2,\ for\,\alpha=1 \tag{3}$$

and for a triangular cross-section:

$$\mu=\frac{m}{V}=\frac{\frac{24}{2}\left\{\frac{\sqrt{3}}{4}b^2 l\right\}+\frac{12}{4}\left\{\frac{\sqrt{3}}{4}b^2\alpha l\right\}}{\left(\alpha+\sqrt{2}\right)^3 l^3}=\frac{\sqrt{3}(12+3\alpha)}{4\left(\alpha+\sqrt{2}\right)^3}\left(\frac{b}{l}\right)^2 \Rightarrow$$
$$\mu=\frac{15\sqrt{3}}{4\left(1+\sqrt{2}\right)^3}\left(\frac{b}{l}\right)^2,\quad for\ \alpha=1 \tag{4}$$

2.2. Derivation of the stiffness matrix

Here we try to find analytical relationships for the stiffness, k_{UC}, Poisson's ratio, ν_{UC}, and yield stress $\sigma_{y,UC}$, of a truncated cube unit cell as functions of elastic modulus, E, Poisson's ratio, ν, and yield stress, σ_y, of the matrix material and the geometrical dimensions (pore size and strut size) of the structure.

A truncated cube unit cell (Fig. 1a) consists of four vertical edges. Due to the symmetry present in the truncated cube structure, we can analyze 1/4 of the unit cell for theoretical study (Fig. 2d). If the total vertical load applied on a unit cell is F, then the vertical load applied on each vertical edge is $F/4$. The noted 1/4 structure consists of six vertices A, C, D, E, F, and H each having six degrees of freedom (DOFs) in space leading to 36 total DOFs for the system. In order to decrease the structure total DOFs, the lower and upper faces of this structure is assumed to be rigid. Due to the intrinsic symmetry of deformation with respect to the planes XZ and ZY, the vertices E and D are only able to move in the 45° plane marked in Fig. 2c. In order to further decrease the DOFs of the system, the hypothetical points G and B which are the midpoints of edges FH and AC are used as DOFs rather than points F, H, A, and C. Again, due to the symmetry of the structure deformation, points B and G are only able to move in the 45° plane depicted in Fig. 2c. Each of the three points G, E, and D are only able to move in the 45° plane leading to three DOFs for each.

The horizontal displacement and force of a point i are denoted as u_i

and F_i, respectively, and the vertical displacement and force of the point are denoted as v_i and G_i, respectively (Fig. 3). The applied moment on each point and its corresponding rotation in the 45° plane are represented by M_i and ϑ_i, respectively. Considering the forces and moments depicted in Fig. 3 and the coordinate system shown in Fig. 2, the external forces and moments acting on points D (denoted by 1), E (denoted by 2), and G (denoted by 3) are as follows:

$$\begin{aligned} \boldsymbol{F}_1 &= F_1(-\boldsymbol{i}-\boldsymbol{j})\frac{\sqrt{2}}{2} \\ \boldsymbol{G}_1 &= -G_1\boldsymbol{k} \\ \boldsymbol{M}_1 &= M_1(-\boldsymbol{i}+\boldsymbol{j})\frac{\sqrt{2}}{2} \end{aligned} \tag{5}$$

$$\begin{aligned} \boldsymbol{F}_2 &= F_2(-\boldsymbol{i}-\boldsymbol{j})\frac{\sqrt{2}}{2} \\ \boldsymbol{G}_2 &= G_2\boldsymbol{k} \\ \boldsymbol{M}_2 &= M_2(\boldsymbol{i}-\boldsymbol{j})\frac{\sqrt{2}}{2} \end{aligned} \tag{6}$$

$$\begin{aligned} \boldsymbol{F}_3 &= F_3(-\boldsymbol{i}-\boldsymbol{j})\frac{\sqrt{2}}{2} \\ \boldsymbol{G}_3 &= G_3\widehat{\boldsymbol{k}} \\ \boldsymbol{M}_3 &= M_3(-\boldsymbol{i}+\boldsymbol{j})\frac{\sqrt{2}}{2} \end{aligned} \tag{7}$$

The force-displacement relationship of the system must have the following form:

$$\begin{Bmatrix} F_1 \\ F_2 \\ F_3 \\ G_1 \\ G_2 \\ G_3 \\ M_1 \\ M_2 \\ M_3 \end{Bmatrix} = \begin{bmatrix} k_{11} & k_{12} & k_{13} & k_{14} & k_{15} & k_{16} & k_{17} & k_{18} & k_{19} \\ k_{21} & k_{22} & k_{23} & k_{24} & k_{25} & k_{26} & k_{27} & k_{28} & k_{29} \\ k_{31} & k_{32} & k_{33} & k_{34} & k_{35} & k_{36} & k_{37} & k_{38} & k_{39} \\ k_{41} & k_{42} & k_{43} & k_{44} & k_{45} & k_{46} & k_{47} & k_{48} & k_{49} \\ k_{51} & k_{52} & k_{53} & k_{54} & k_{55} & k_{56} & k_{57} & k_{58} & k_{59} \\ k_{61} & k_{62} & k_{63} & k_{64} & k_{65} & k_{66} & k_{67} & k_{68} & k_{69} \\ k_{71} & k_{72} & k_{73} & k_{74} & k_{75} & k_{76} & k_{77} & k_{78} & k_{79} \\ k_{81} & k_{82} & k_{83} & k_{84} & k_{85} & k_{86} & k_{87} & k_{88} & k_{89} \\ k_{91} & k_{92} & k_{93} & k_{94} & k_{95} & k_{96} & k_{97} & k_{98} & k_{99} \end{bmatrix} \begin{Bmatrix} u_1 \\ u_2 \\ u_3 \\ v_1 \\ v_2 \\ v_3 \\ \theta_1 \\ \theta_2 \\ \theta_3 \end{Bmatrix} \tag{8}$$

where the stiffness matrix elements k_{ij} have to be found in order to obtain the displacements, rotations, forces, and moments as functions of the applied force F from which different elastic properties of unit cell can be found. The vertices of the unit cell are considered rigid connections. The displacements of each DOF can be considered as the superpositions of displacements due to forces on all nine DOFs. In other words, by separately displacing each DOF (say DOF i) for unity while the other DOFs are kept fixed, the moments and forces required at all DOFs to maintain the equilibrium are obtained. These forces and moments construct the elements of the i th column of the stiffness matrix given in Eq. (8). For example, if we displace the fifth DOF for unity and keep the other DOFs fixed, the required forces and moments at the nine DOFs to cause such a deformation construct the elements of the fifth column of the stiffness matrix. In the 2D deformation of a cantilever beam, the deformation of the free end of the beam can be considered as the sum of four different types of displacements and rotations including axial tension/compression (u), lateral displacement (v), bending rotation (θ) and torsional rotation (φ), see Fig. 4. The forces and moments necessary for creating such pure displacements and rotations are depicted in Fig. 5. The detailed procedure of obtaining the elements of the stiffness matrix is provided in the electronic Appendix accompanying the paper. The final force-displacement relationship is (See appendix for details):

$$\begin{bmatrix} \frac{18EI}{l^3}+\frac{AE}{2l}+\frac{12EI}{m^3} & -\frac{12EI}{m^3} & \frac{\sqrt{2}AE}{2l}-\frac{6\sqrt{2}EI}{l^3} & 0 & \frac{\sqrt{2}AE}{2l}-\frac{6\sqrt{2}EI}{l^3} & 0 & -\frac{6EI}{m^2} & \frac{6EI}{m^2}-\frac{6\sqrt{2}EI}{l^2} & 0 \\ -\frac{12EI}{m^3} & \frac{18EI}{l^3}+\frac{AE}{2l}+\frac{12EI}{m^3} & 0 & \frac{\sqrt{2}AE}{2l}-\frac{6\sqrt{2}EI}{l^3} & 0 & -\frac{\sqrt{2}AE}{2l}+\frac{6\sqrt{2}EI}{l^3} & \frac{6EI}{m^2} & -\frac{6EI}{m^2} & 0 \\ 0 & 0 & \frac{AE}{l}+\frac{AE}{m}+\frac{12EI}{l^3} & \frac{AE}{m} & -\frac{AE}{l}-\frac{12EI}{l^3} & 0 & 0 & 0 & \frac{6EI}{l^2} \\ \frac{\sqrt{2}AE}{2l}-\frac{6\sqrt{2}EI}{l^3} & 0 & \frac{AE}{m} & \frac{AE}{l}+\frac{AE}{m}+\frac{12EI}{l^3} & 0 & -\frac{12EI}{l^3}+\frac{AE}{l} & \frac{6EI}{l^2} & 0 & 0 \\ 0 & -\frac{\sqrt{2}AE}{2l}+\frac{6\sqrt{2}EI}{l^3} & 0 & 0 & \frac{AE}{l}+\frac{12EI}{l^3} & 0 & 0 & 0 & 0 \\ -\frac{6\sqrt{2}EI}{l^2}+\frac{6EI}{m^2} & \frac{6EI}{m^2} & 0 & \frac{6EI}{l^2} & 0 & \frac{4EI}{m}-\frac{GJ}{2l}+\left(\sqrt{6}+2\sqrt{3}\right)\frac{EI}{l} & -\frac{2EI}{m} & \frac{4EI}{m}-\frac{GJ}{2l}+\left(\sqrt{6}+2\sqrt{3}\right)\frac{EI}{l} & 0 \\ -\frac{6EI}{m^2} & -\frac{6\sqrt{2}EI}{l^2}+\frac{6EI}{m^2} & 0 & -\frac{6EI}{l^2} & 0 & -\frac{2EI}{m} & \frac{4EI}{m}-\frac{GJ}{2l}+\left(\sqrt{6}+2\sqrt{3}\right)\frac{EI}{l} & 0 & 0 \\ 0 & \frac{6\sqrt{2}EI}{l^2} & 0 & -\frac{6EI}{l^2} & 0 & 0 & 0 & \frac{GJ}{2l}-\left(\frac{\sqrt{6}+2\sqrt{3}}{2}\right)\frac{EI}{l} & 0 \\ 0 & 0 & 0 & 0 & 0 & 0 & 0 & 0 & -1 \end{bmatrix} \begin{Bmatrix} u_1 \\ u_2 \\ v_1 \\ v_2 \\ v_3 \\ \theta_1 \\ \theta_2 \\ F_3 \\ M_3 \end{Bmatrix} = \begin{Bmatrix} 0 \\ 0 \\ 0 \\ 0 \\ F/4 \\ 0 \\ 0 \\ 0 \end{Bmatrix} \tag{A29}$$

2.3. The elastic properties

The unknown elements in the vector on the right side of Eq. (A29) can be simply obtained by inverting the new stiffness matrix and multiplying it by the new force vector. Using the obtained unknowns, it is possible to calculate the stiffness, Poisson's ratio, and yield stress as functions of the geometrical and material properties m, l, E, G, and strut dimension of the structure. The stiffness of the structure is found by dividing F by v_3. The Poisson's ratio can be obtained by dividing displacement u_2 by v_3. It was observed that if the relationships for stiffness and Poisson's ratio are expressed as functions of area moment of inertia and polar area moment of inertia, the obtained formulas become very lengthy exceeding two pages. Therefore it was decided to substitute I and J with their corresponding values for each cross-section type.

2.3.1. Stiffness

The stiffness was obtained using the following formula

$$k_{UC} = \frac{F}{v_3} \tag{9}$$

For the circular cross-section, with strut radius of r, the obtained normalized stiffness was

$$\frac{k_{UC}}{E} = \frac{4(9)\pi}{\sqrt{2}+\alpha}\left(\frac{r}{l}\right)^4 \frac{\left(2 - 4.5\alpha + 2\sqrt{3}\alpha + \sqrt{6}\alpha - \frac{G}{E}\alpha\right)\left[1+\left(\frac{r}{l}\right)^2\right](\sqrt{2}+\alpha)l}{\left[2+\alpha\left(2\sqrt{3}+\sqrt{6}\right)-\frac{G}{E}\alpha\right]\left[1+9\left(1+\alpha+\alpha\left(\frac{r}{l}\right)^2\right)\left(\frac{r}{l}\right)^2\right] - \frac{81}{2}\alpha^2\left(\frac{r}{l}\right)^2\left(1+\left(\frac{r}{l}\right)^2\right)} \tag{10}$$

where α has been used for simplifying the expression and, as said before, is defined as $m = \alpha l$. The parameter $\sqrt{2}l + m = (\sqrt{2}+\alpha)l$ is the unit cell dimension in the three directions. By setting $\alpha = 1$, (i.e. an equilateral structure) we have:

$$\frac{k_{UC}}{E} = \frac{10.41032\left(\frac{G}{E} - 2 - \sqrt{2}\right)\left[\left(\frac{r}{l}\right)^2 + 1\right]\left(\frac{r}{l}\right)^4(\sqrt{2}+1)l}{9\left(\frac{r}{l}\right)^2\left[\left(\frac{r}{l}\right)^2 + 1\right] + \left(\frac{2G}{E} - 15.827182\right)\left[\frac{1}{9} + \left(\frac{r}{l}\right)^2\left(\left(\frac{r}{l}\right)^2 + 2\right)\right]} \tag{11}$$

For square cross-section with cross-section side length of b, the obtained normalized stiffness was

$$\frac{k_{UC}}{E} = \frac{4}{\sqrt{2}+\alpha}\left(\frac{b}{l}\right)^4 \frac{\left(2 - 4.5\alpha + 2\sqrt{3}\alpha + \sqrt{6}\alpha - \frac{G}{E}\alpha\right)\left[3+\left(\frac{b}{l}\right)^2\right](\sqrt{2}+\alpha)l}{\left[2+\alpha\left(2\sqrt{3}+\sqrt{6}\right)-\frac{G}{E}\alpha\right]\left[1+\left(3+3\alpha+\left(\frac{b}{l}\right)^2\alpha\right)\left(\frac{b}{l}\right)^2\right] - \frac{9}{2}\alpha^2\left(\frac{b}{l}\right)^2\left(3+\left(\frac{b}{l}\right)^2\right)} \tag{12}$$

By setting $\alpha = 1$, Eq. (12) decreases to

$$\frac{k_{UC}}{E} = \frac{3.3137085\left(\frac{G}{E} - 2 - \sqrt{2}\right)\left[\left(\frac{b}{l}\right)^2 + 3\right]\left(\frac{b}{l}\right)^4(\sqrt{2}+1)l}{9\left(\frac{b}{l}\right)^2\left[\left(\frac{b}{l}\right)^2 + 3\right] + \left(\frac{2G}{E} - 15.82718\right)\left[1+\left(\frac{b}{l}\right)^2\left(\left(\frac{b}{l}\right)^2 + 6\right)\right]} \tag{13}$$

For equilateral triangular cross-section with cross-section side length of b, the obtained normalized stiffness was

$$\frac{k_{UC}}{E} = \frac{\sqrt{3}}{\sqrt{2}+\alpha}\left(\frac{b}{l}\right)^4 \frac{\left(2 - 4.5\alpha + 2\sqrt{3}\alpha + \sqrt{6}\alpha - \frac{G}{E}\alpha\right)\left(6+\left(\frac{b}{l}\right)^2\right)(\sqrt{2}+\alpha)l}{\left[2+\left(2\sqrt{3}+\sqrt{6}\right)\alpha-\frac{G}{E}\alpha\right]\left[4+6\left(\frac{b}{l}\right)^2+6\left(\frac{b}{l}\right)^2\alpha+\alpha\left(\frac{b}{l}\right)^4\right] - 9\alpha\left(\frac{b}{l}\right)^2\left(2+3\alpha+\frac{\alpha}{2}\left(\frac{b}{l}\right)^2\right)} \tag{14}$$

By setting $\alpha = 1$, i.e. for a unit cell with equal edge lengths, Eq. (14) is simplified to

$$\frac{k_{UC}}{E} = \frac{0.7174389\left(\frac{G}{E} - 2 - \sqrt{2}\right)\left[\left(\frac{b}{l}\right)^2 + 6\right]\left(\frac{b}{l}\right)^4(\sqrt{2}+1)l}{9\left(\frac{b}{l}\right)^2\left[0.5\left(\frac{b}{l}\right)^2 + 5\right] + \left(\frac{G}{E} - 7.91359\right)\left[4+\left(\frac{b}{l}\right)^2\left(\left(\frac{b}{l}\right)^2 + 12\right)\right]} \tag{15}$$

2.3.2. Poisson's ratio

Poisson's ratio was obtained using the following formula

$$\nu_{UC} = \frac{\sqrt{2}}{2}\frac{u_2}{v_3} \tag{16}$$

The coefficient $\frac{\sqrt{2}}{2}$ was put before u_2, because u_2 is representative of horizontal displacement in the 45° plane and not in the direction perpendicular to the unit cell side planes. For the circular cross-section, the Poisson's ratio was found to be

$$\nu_{UC}=\frac{1}{2}\frac{\left(2+\left(2\sqrt{3}+\sqrt{6}\right)\alpha-\frac{G}{E}\alpha\right)\left(1-3\left(\frac{r}{l}\right)^2\right)+18\left(\frac{r}{l}\right)^2\alpha}{\left(2+\left(2\sqrt{3}+\sqrt{6}\right)\alpha-\frac{G}{E}\alpha\right)\left[1+9\left(\frac{r}{l}\right)^2\left(1+\alpha+\alpha\left(\frac{r}{l}\right)^2\right)\right]-\frac{81}{2}\left(\frac{r}{l}\right)^2\alpha^2\left[\left(\frac{r}{l}\right)^2+\frac{17}{9}\right]} \tag{17}$$

For $\alpha=1$, Eq. (17) reduces to

$$\nu_{UC}=\frac{\left(\frac{G}{E}-7.9135913\right)\left[1-3\left(\frac{r}{l}\right)^2\right]-18\left(\frac{r}{l}\right)^2}{\left(\frac{2G}{E}-15.82718\right)\left[1+9\left(\frac{r}{l}\right)^2\left(\left(\frac{r}{l}\right)^2+2\right)\right]+81\left(\frac{r}{l}\right)^2\left(\frac{17}{9}+\left(\frac{r}{l}\right)^2\right)} \tag{18}$$

For square cross-section with cross-section side length of b, the obtained Poisson's ratio was

$$\nu_{UC}=\frac{1}{2}\frac{\left(2+\left(2\sqrt{3}+\sqrt{6}\right)\alpha-\frac{G}{E}\alpha\right)\left(1-\left(\frac{b}{l}\right)^2\right)+6\alpha\left(\frac{b}{l}\right)^2}{\left(2+\left(2\sqrt{3}+\sqrt{6}\right)\alpha-\frac{G}{E}\alpha\right)\left[1+\left(\frac{b}{l}\right)^2\left(3+3\alpha+\alpha\left(\frac{b}{l}\right)^2\right)\right]-\frac{9}{2}\left(\frac{b}{l}\right)^2\alpha^2\left[\left(\frac{b}{l}\right)^2+\frac{17}{3}\right]} \tag{19}$$

For $\alpha=1$, Eq. (19) simplifies to

$$\nu_{UC}=\frac{\left(\frac{G}{E}-7.91359\right)\left[1-\left(\frac{b}{l}\right)^2\right]-6\left(\frac{b}{l}\right)^2}{\left(\frac{2G}{E}-15.82718\right)\left[1+\left(\frac{b}{l}\right)^2\left(\left(\frac{b}{l}\right)^2+6\right)\right]+9\left(\frac{b}{l}\right)^2\left(\frac{17}{3}+\left(\frac{b}{l}\right)^2\right)} \tag{20}$$

For the triangular cross-section and for $\alpha=1$, we have:

$$\nu_{UC}=\frac{\left(\frac{G}{E}-1.91359\right)\left[\left(\frac{b}{l}\right)^2-2\right]+12}{\left(3.4135-\frac{G}{E}\right)\left(4+12\left(\frac{b}{l}\right)^2+\left(\frac{b}{l}\right)^4\right)+3\left(6+\left(\frac{b}{l}\right)^2\right)} \tag{21}$$

2.4. Yield stress

First, the yield stress of the structure is found assuming that the corners of the vertical struts, i.e. vertices E and D in Fig. 2, are the locations where yielding occurs initially. In order to obtain the stress at point E, first it is necessary to calculate the moments applied by edges EF and EH. Assume a deformation where a load F is applied on the top rigid surface and the displacements in the DOFs of point E are u_2, v_2 and θ_2 where the vertical displacement of points F and H are v_3. By multiplying Eqs. (A2) and (A3) by v_2-v_3, Eqs. (A9) and (A10) by u_2, Eq. (A20-A-22) by θ_2, and adding the resulting moment expressions, the total moment applied on point E is calculated as

$$\sum \boldsymbol{M}=\left\{(v_3-v_2)\frac{\sqrt{2}}{2}\frac{6EI}{l^2}+u_2\frac{\sqrt{2}}{2}\frac{\sqrt{2}}{2}\frac{6EI}{l^2}+u_2\frac{6EI}{2l^2}-\theta_2\frac{4EI}{l}\frac{\sqrt{3}}{2}\frac{1}{2}+\theta_2\frac{GJ}{l}\frac{1}{2}\frac{\sqrt{2}}{2}-\theta_2\frac{4EI}{l}\frac{\sqrt{3}}{2}\frac{\sqrt{2}}{2}\right\}\boldsymbol{i}$$
$$+\left\{(v_2-v_3)\frac{\sqrt{2}}{2}\frac{6EI}{l^2}-u_2\frac{6EI}{2l^2}-u_2\frac{\sqrt{2}}{2}\frac{\sqrt{2}}{2}\frac{6EI}{l^2}+\theta_2\frac{4EI}{l}\frac{\sqrt{3}}{2}\frac{\sqrt{2}}{2}+\theta_2\frac{4EI}{l}\frac{\sqrt{3}}{2}\frac{1}{2}-\theta_2\frac{GJ}{l}\frac{1}{2}\frac{\sqrt{2}}{2}\right\}\boldsymbol{j}$$
$$+\left\{u_2\frac{\sqrt{2}}{2}\frac{\sqrt{2}}{2}\frac{6EI}{l^2}-u_2\frac{\sqrt{2}}{2}\frac{\sqrt{2}}{2}\frac{6EI}{l^2}-\frac{1}{2}\theta_2\frac{4EI}{l}\frac{\sqrt{3}}{2}-\theta_2\frac{GJ}{l}\frac{1}{2}\frac{\sqrt{2}}{2}+\frac{1}{2}\theta_2\frac{4EI}{l}\frac{\sqrt{3}}{2}+\theta_2\frac{GJ}{l}\frac{1}{2}\frac{\sqrt{2}}{2}\right\}\boldsymbol{k}$$
$$=\left((v_3-v_2)\frac{3\sqrt{2}EI}{l^2}+u_2\frac{6EI}{l^2}-\theta_2\frac{\left(\sqrt{6}+\sqrt{3}\right)EI}{l}+\theta_2\frac{\sqrt{2}}{4}\frac{GJ}{l}\right)\boldsymbol{i}+\left((v_2-v_3)\frac{3\sqrt{2}EI}{l^2}-u_2\frac{6EI}{l^2}+\theta_2\frac{\left(\sqrt{6}+\sqrt{3}\right)EI}{l}-\frac{\sqrt{2}}{4}\theta_2\frac{GJ}{l}\right)\boldsymbol{j} \tag{22}$$

from which it can be concluded that the moment acting on point E is

$$M=(v_3-v_2)\frac{6EI}{l^2}+u_2\frac{6\sqrt{2}EI}{l^2}-\theta_2\frac{\left(2\sqrt{3}+\sqrt{6}\right)EI}{l}+\theta_2\frac{GJ}{2l} \tag{23}$$

Obtaining u_2, v_2 and θ_2 from the compliance matrix (Eq. (A29)) and substituting them into Eq. (23) and setting $\alpha=1$ gives

$$M=\frac{-\sqrt{2}\left(1+\left(\frac{r}{l}\right)^2\right)\left(\sqrt{2}+\sqrt{3}+\sqrt{6}-\frac{4\pi}{3}\right)F}{32l\left\{5+2\frac{G}{E}-4\sqrt{3}-2\sqrt{6}+5\left(\frac{r}{l}\right)^2+2\frac{G}{E}\left(\frac{r}{l}\right)^2-4\sqrt{3}\left(\frac{r}{l}\right)^2-2\sqrt{6}\left(\frac{r}{l}\right)^2\right\}} \tag{24}$$

which simplifies to

$$M=\frac{\left(\frac{4\pi}{3}-2-\sqrt{6}-2\sqrt{3}\right)F}{32l\left(5-4\sqrt{3}-2\sqrt{6}+2\frac{G}{E}\right)} \tag{25}$$

Considering $\sigma_y=\frac{Mc}{I}$, where c is the distance between the neural axis of the strut and its outer fiber, the maximum stress can be found by multiplying Eq. (24) by $\frac{4r}{\pi r^4}$ and adding it to the axial compressive stress applied on the vertical edge ED, $\frac{F}{4\pi r^2}$, which gives

$$\sigma_{max}=\frac{\left(\frac{4\pi}{3}-2-\sqrt{6}-2\sqrt{3}\right)}{8\pi\left(5-4\sqrt{3}-2\sqrt{6}+2\frac{G}{E}\right)}\frac{F}{r^3l}+\frac{F}{4\pi r^2} \tag{26}$$

The stress applied on the unit cell is $\frac{F}{(\sqrt{2}+\alpha)^2l^2}$ where $(\sqrt{2}+\alpha)l$ is the dimension of the unit cell. Using $\sigma_{y,UC}=\frac{F}{(\sqrt{2}+\alpha)^2l^2}$ and $\sigma_y=\sigma_{max}$, the normalized yield stress of a truncated cube unit cell with circular cross-section is:

$$\frac{\sigma_{y,UC}}{\sigma_y}=\frac{8\pi\left(\frac{r}{l}\right)^2}{\left(\sqrt{2}+\alpha\right)^2\left[\frac{\left(\frac{4\pi}{3}-2-\sqrt{6}-2\sqrt{3}\right)}{2\left(5-4\sqrt{3}-2\sqrt{6}+2\frac{G}{E}\right)}\frac{1}{rl}+1\right]} \tag{27}$$

This expression gives a negative value showing the compressive yield stress.

Now, we find the yield stress of the structure assuming that the *inclined* sides of the intersection of the inclined and vertical struts (i.e. points E and D) are the locations which yield first. In order to obtain the stress at point E, first it is necessary to calculate the moments applied on it. By multiplying Eq. (A2) by v_2-v_3, Eq. (A9) by u_2, M in Eq. (A20) by $\frac{\theta_2}{2}$, and T in Eq. (A20) by θ_2, and adding the resulting moment expressions, the total moment applied on edge EF is calculated as

$$\begin{aligned}\sum \boldsymbol{M}&=\left\{u_2\frac{\sqrt{2}}{2}\frac{\sqrt{2}}{2}\frac{6EI}{l^2}-\frac{\theta_2}{2}\frac{1}{2}\frac{4EI}{l}\frac{\sqrt{3}}{2}+\theta_2\frac{GJ}{l}\frac{1}{2}\frac{\sqrt{2}}{2}\right\}\boldsymbol{i}+\left\{(v_2-v_3)\frac{\sqrt{2}}{2}\frac{6EI}{l^2}-u_2\frac{6EI}{2l^2}+\frac{\theta_2}{2}\frac{4EI}{l}\frac{\sqrt{3}}{2}\frac{\sqrt{2}}{2}\right\}\boldsymbol{j}\\&+\left\{u_2\frac{\sqrt{2}}{2}\frac{\sqrt{2}}{2}\frac{6EI}{l^2}-\frac{\theta_2}{2}\frac{1}{2}\frac{4EI}{l}\frac{\sqrt{3}}{2}-\theta_2\frac{GJ}{l}\frac{1}{2}\frac{\sqrt{2}}{2}\right\}\boldsymbol{k}\\&=\left(u_2\frac{3EI}{l^2}-\theta_2\frac{EI}{l}\frac{\sqrt{3}}{2}+\theta_2\frac{GJ}{l}\frac{\sqrt{2}}{4}\right)\boldsymbol{i}+\left((v_2-v_3)\frac{3\sqrt{2}EI}{l^2}-u_2\frac{3EI}{l^2}+\theta_2\frac{EI}{l}\frac{\sqrt{6}}{2}\right)\boldsymbol{j}\\&+\left(u_2\frac{3EI}{l^2}-\theta_2\frac{EI}{l}\frac{\sqrt{3}}{2}-\theta_2\frac{GJ}{l}\frac{\sqrt{2}}{4}\right)\boldsymbol{k}\end{aligned} \tag{28}$$

The unit vector of edge EF is $u_{EF}=\left(\frac{\sqrt{2}}{2},0,\ -\frac{\sqrt{2}}{2}\right)$. Therefore, projection of the moment vector given in Eq. (28) onto edge EF is

$$\boldsymbol{M}_{EF}=\frac{\sqrt{2}}{2}\left(u_2\frac{3EI}{l^2}-\theta_2\frac{EI}{l}\frac{\sqrt{3}}{2}+\theta_2\frac{GJ}{l}\frac{\sqrt{2}}{4}\right)-\frac{\sqrt{2}}{2}\left(u_2\frac{3EI}{l^2}-\theta_2\frac{EI}{l}\frac{\sqrt{3}}{2}-\theta_2\frac{GJ}{l}\frac{\sqrt{2}}{4}\right)=\theta_2\frac{GJ}{2l} \tag{29}$$

from which the perpendicular component of the moment vector with respect to edge EF is

$$\boldsymbol{M}_{\perp EF}=\sqrt{27u_2^2\left(\frac{EI}{l^2}\right)^2+3\theta_2^2\left(\frac{EI}{l}\right)^2+18(v_2-v_3)^2\left(\frac{EI}{l^2}\right)^2} \tag{30}$$

which for $\alpha=1$ gives a very lengthy expression for yield stress that is not stated here. Unlike edge ED, the axial load applied on edge EF is not simply $\frac{F}{4\pi r^2}$, because the top edge also imposes horizontal force on point E of this edge. By multiplying Eq. (A2) by v_2-v_3, Eq. (A9) by u_2, Eq. (A21) by θ_2, and adding the resulting moment expressions, the total force applied on point E is calculated as

$$\begin{aligned}\sum \boldsymbol{F}&=\left\{(v_2-v_3)\frac{1}{2}\left(\frac{EA}{l}-\frac{12EI}{l^3}\right)+u_2\left(\frac{\sqrt{2}EA}{4l}+\frac{3\sqrt{2}EI}{l^3}\right)-\theta_2\frac{6EI}{l^2}\frac{\sqrt{3}}{2}\frac{1}{\sqrt{3}}\right\}\boldsymbol{i}+\left\{u_2\frac{6\sqrt{2}EI}{l^3}-\theta_2\frac{6EI}{l^2}\frac{\sqrt{3}}{2}\frac{1}{\sqrt{3}}\right\}\boldsymbol{j}\\&+\left\{(v_2-v_3)\frac{1}{2}\left(-\frac{EA}{l}-\frac{12EI}{l^3}\right)+u_2\left(-\frac{\sqrt{2}EA}{4l}+\frac{3\sqrt{2}EI}{l^3}\right)-\theta_2\frac{6EI}{l^2}\frac{\sqrt{3}}{2}\frac{1}{\sqrt{3}}\right\}\boldsymbol{k}\\&=\left((v_2-v_3)\left(\frac{EA}{2l}-\frac{6EI}{l^3}\right)+u_2\left(\frac{\sqrt{2}EA}{4l}+\frac{3\sqrt{2}EI}{l^3}\right)-\theta_2\frac{3EI}{l^2}\right)\boldsymbol{i}\\&+\left(u_2\frac{6\sqrt{2}EI}{l^3}-\theta_2\frac{3EI}{l^2}\right)\boldsymbol{j}\\&+\left((v_2-v_3)\left(-\frac{EA}{2l}-\frac{6EI}{l^3}\right)+u_2\left(-\frac{\sqrt{2}EA}{4l}+\frac{3\sqrt{2}EI}{l^3}\right)-\theta_2\frac{3EI}{l^2}\right)\boldsymbol{k}\end{aligned} \tag{31}$$

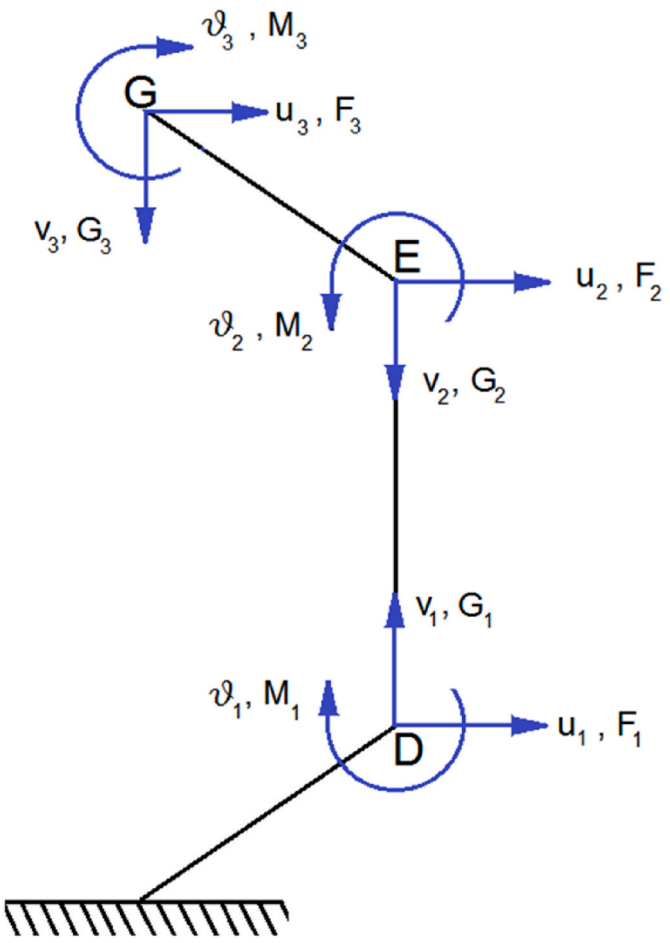

Fig. 3. Degrees of freedom of points G, E, and D in the 45° plane.

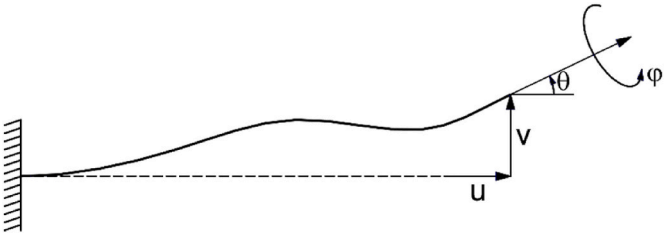

Fig. 4. Cantilever beam having four types of displacement/rotations at its free end [40].

Projection of the force vector given in Eq. (31) onto edge EF is

$$\boldsymbol{F}_{EF} = \frac{\sqrt{2}}{2}\left((v_2 - v_3)\left(\frac{EA}{2l} - \frac{6EI}{l^3}\right) + u_2\left(\frac{\sqrt{2}EA}{4l} + \frac{3\sqrt{2}EI}{l^3}\right) - \theta_2\frac{3EI}{l^2}\right)$$
$$-\frac{\sqrt{2}}{2}\left((v_2 - v_3)\left(-\frac{EA}{2l} - \frac{6EI}{l^3}\right) + u_2\left(-\frac{\sqrt{2}EA}{4l} + \frac{3\sqrt{2}EI}{l^3}\right) - \theta_2\frac{3EI}{l^2}\right)$$
$$= (v_2 - v_3)\left(\frac{\sqrt{2}EA}{2l}\right) + u_2\left(\frac{EA}{2l}\right) \tag{32}$$

which for $\alpha = 1$ becomes

$$F_{EF} = \frac{-F\left(2.5\sqrt{2} - 2\sqrt{6} - 2\sqrt{3} + \sqrt{2}\ \frac{G}{E}\right)}{\left(30 + 12\frac{G}{E} - 24\sqrt{3} - 12\sqrt{6}\right)\left[1 + \left(\frac{r}{l}\right)^2\right]} \Rightarrow \quad F_{EF} = \frac{-F}{6\sqrt{2}\left[1 + \left(\frac{r}{l}\right)^2\right]} \tag{33}$$

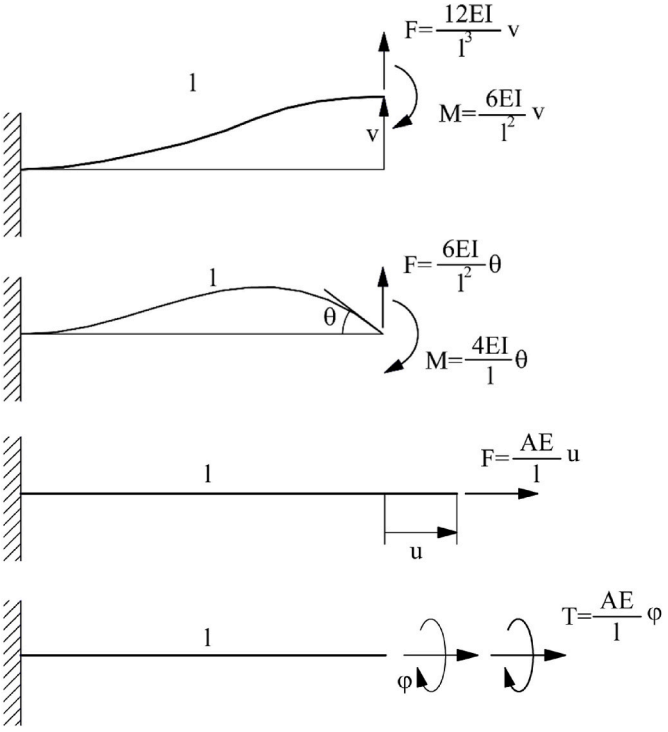

Fig. 5. Forces and moments necessary to be applied to cause the illustrated deformations.

Table 1
Mechanical properties of the PLA material under tensile loading.

Density (kg/m^3)	Young's modulus (GPa)	Ultimate tensile strength (MPa)	Poisson's ratio
1240	3.7	57	0.36

Multiplying Eq. (30) by $\frac{4r}{\pi r^4}$ and Eq. (33) by $\frac{1}{\pi r^2}$ gives the maximum stress of the structure assuming that the inclined strut side of the intersection of vertical and inclined struts are the most susceptible locations to yielding. The obtained expression for yield stress is very lengthy and is not stated here. However, in the following, its results are plotted and compared to other results.

2.5. Finite element (FE) modeling of unit cells using beam elements

The main mechanism of deformation in the truncated cube unit cell is bending of the struts making the beam elements the natural choice for modelling them. Beam elements are computationally inexpensive and can be used to compose models with a large number of cells [49]. The cell edges were discretized using standard Timoshenko beam elements (element type 189 in ANSYS) that uses linear interpolation (two-node linear beam) and allows for transverse shear deformation. Considering transverse shear deformation becomes more important in struts with higher thickness to length ratios.

All the struts in the open-cell porous structures were represented mechanically by beams that were rigidly connected in vertices. The material considered for the analyses was polylactic acid (PLA). In all the calculations, the cell edge material was assumed to be linear elastic, with mechanical properties given in Table 1.

The static nonlinear implicit solver available in ANSYS FE code (United States) was used for the calculations. The FE model (Fig. 6) consisted of eleven struts similar to the configuration considered for analytical investigation (thick lines in Fig. 2a). In this structure, all the DOFs of the lowermost struts were fixed in the space, and the top struts

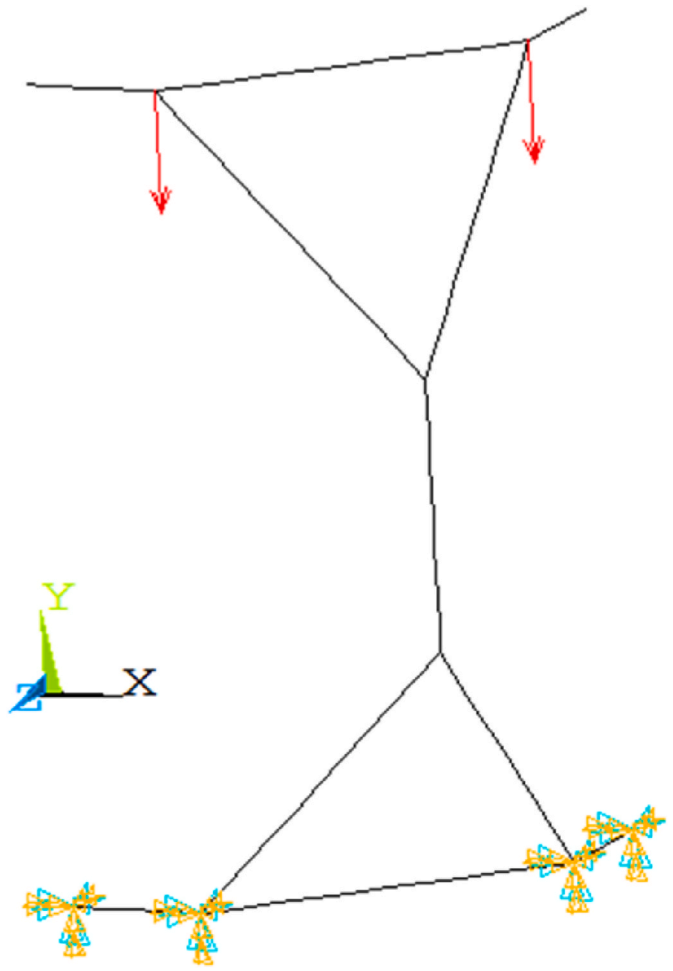

Fig. 6. The loads and boundary conditions used in the FE truncated cube model.

were only allowed to move vertically. Two concentred forces of $\frac{F}{8}$ were applied on top points F and H of the simple structure (Fig. 2a).The effective stiffness was calculated by dividing the applied force by the resulting displacement in the Y direction; and Poisson's ratios were calculated by dividing the negative value of the lateral displacement by the axial displacement.

2.6. Finite element modeling of sandwich panels and unit cells using volumetric elements

The commercial ABAQUS software (V 6.14. Dassault systems, France) was used to model the compression tests on three types of unit cells with different strut radii (2 mm, 3 mm, and 4 mm). Dynamic implicit analysis was used to predict the unit cells' behaviour in large deformation regime. The application mode in the ABAQUS was set to quasi-static, which decreases simulation time and increases the accuracy of results.

Fig. 7c demonstrates the engineering stress-strain curves of three similar doge-bone PLA specimens under tensile test. As illustrated in this figure, the material's behavior is elastic-plastic, and after the yielding point, a plateau regime is observed. The stress-strain data were imported into ABAQUS using the calibration tool, and ABAQUS calculated all the required parameters for modeling elastic-plastic behavior. The measured mechanical properties of the PLA material are listed in Table 1. To model damage in truncated cube unit cells, the ductile damage option in ABAQUS was considered (with parameters listed in Table 2). The fracture energy value was taken from Noori's work [50] which reports the fracture energy for interlayer fracture of specimens with different deposition heights.

Fig. 7a depicts the discritized geometry of the truncated cube unit cell with struct radius of 2 mm. The top plate is allowed to move in the Y direction and it is restricted in all other directions, while the bottom plate is fixed in all directions. Both plates are considered to be rigid bodies; hence their force and displacement values can be obtained from those of defined reference points. The general contact type was defined between the upper and lower plates and the truncated cube unit cells. Linear hexahedron (C3D8R) elements were employed for discretizing both the upper and lowermost plates, and linear tetrahedron C3D4 elements were used for the unit cell.

In the next set of simulations, the truncated cube unit cell was utilized as a the core material for sandwich panels (Fig. 7b) and their energy absorption capability was studied. Aluminum face sheets were considered for the sandwich structure, and their elastic-plastic mechanical behaviour was modeled using the Johnson-Cook material model [51]. The larger bed plate at the bottom side as well as the loading pin were considered as rigid bodies. Both the lower plates (rigid and aluminum plates) were restricted in all directions. The loading pin was allowed to move in the Y direction only, and it was constrained in all other directions. The main reason for using a sandwich structure supported by a rigid back plate and under the impact of a pin was to model the frontal pole crash, especially when the sandwich panel is used as an energy absorption structure in cars [52,53].

General contact was defined between different parts. *Tie* constraint was defined between the unit cells and the aluminum plates. The loading pin was moved downwards until a fracture occurred in a unit cell. The criteria which take into account the damage initiation (and fracture) of the unit cell is the ductile damage initiation criterion (DUCTCRT). DUCTCTR ranges from 0 to 1; when it reaches 1, the damage is initiated [54]. The main reason for switching from ANSYS for simulating beam elements to ABAQUS for volumetric elements modeling was the capability of ABAQUS in importing fracture energy for interlayer fracture energy of specimens and its ability to show the ductile damage initiation criterion (DUCTCRT), which are essential for the present nonlinear simulation. Linear hexahedron (C3D8R) element type was used to discretize the plates, while linear tetrahedron (C3D4) element type was implemented to discretize the unit cells and loading pin.

Three types of sandwich panels with aluminum face sheets and uniform unit cell density distribution (with different strut radii of 2 mm, 3 mm, and 4 mm), and four types of sandwich structures with graded cores were considered. In order to examine the effect of different core types, the overall dimensions of sandwich structures were kept equal in all the cases: the sandwich structures were 300 mm in length, 50 mm in depth, and 50 mm in height; the truncated cube cells were 40 mm in height; and the aluminum face sheets were 5 mm thick. Moreover, the distance between two neighboring truncated cube cells (the distance between symmetry planes of the cells) was considered to be 1.5 times the height of the truncated cube cell (i.e. 60 mm). Different graded sandwich panel configurations examined in this study are demonstrated in Fig. 8, and their specifics are listed in Table 3.

2.7. Experiments

Experimental tests were also carried out to evaluate the validity of the analytical and numerical results. Unit cells with different strut radii (2 mm, 3 mm, and 4 mm) but with equal strut lengths (15 mm) were produced using fused deposition modelling (FDM) additively manufacturing technique (Fig. 9). Three samples were fabricated for each geometry. Makerbot replicator 5th generation was used for production of the samples using light brown PLA filaments. Layer thickness of 100 μm, infill density of 100%, and nozzle diameter of 0.4 mm was used for the printing process. In addition to truncated cube unit cells, cylindrical specimens with 12.7 mm diameter and 25.4 mm length (according to standard ASTM D695, ISO 604) were produced and tested.

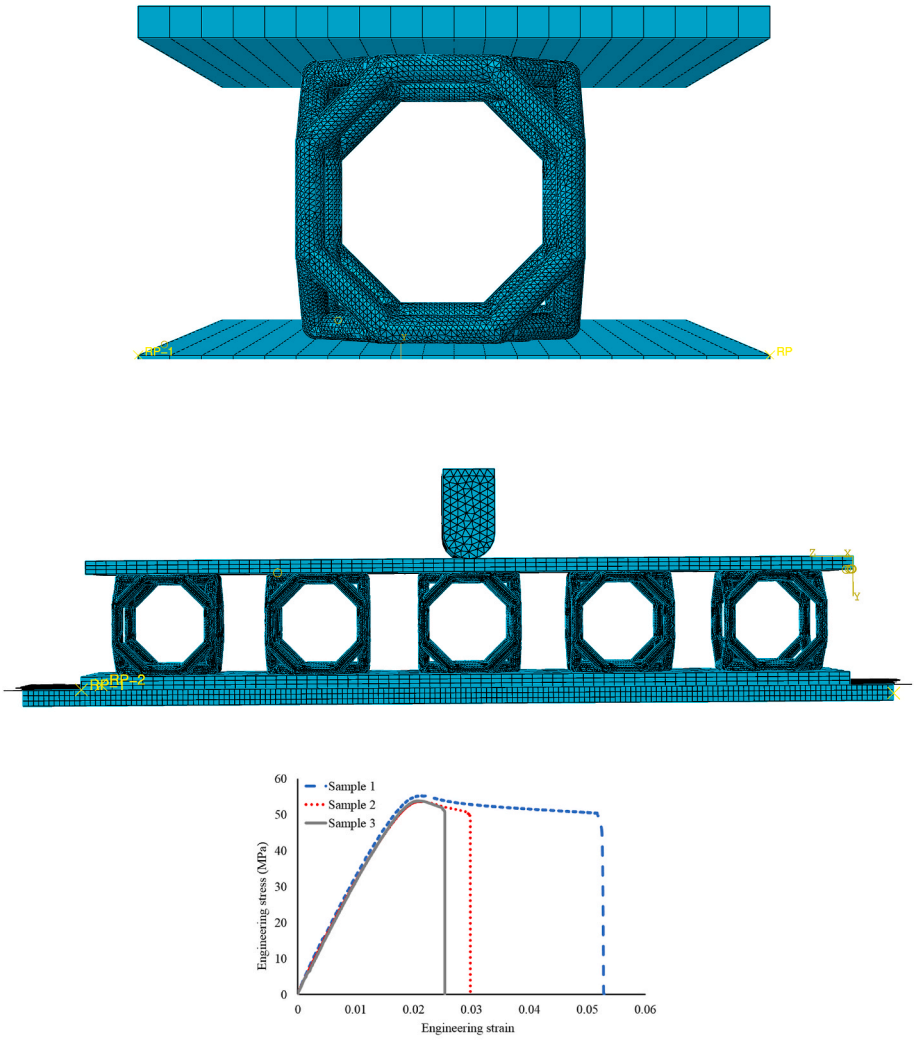

(c)

Fig. 7. Configuration of (a) truncated cube unit cell model under compression, (b) sandwich panel with uniform distribution of truncated cube unit cells. (c) Stress-strain of the bulk PLA material used for FEM modelling.

Table 2
Parameters required for modeling ductile damage in PLA.

Fracture strain	Fracture energy (mJ/mm^2) [50]	Stress triaxiality
0.036	5	0.33

All the cylindrical and truncated cube samples were mechanically tested under compression using a static mechanical testing machine (INSTRON 5985, load cell: 10 kN). The stiffness and yield stress of each truncated cube sample was obtained from the corresponding load-displacement curve and then divided by the elastic modulus and yield stress of the cylindrical specimens to give normalized values.

3. Results

3.1. Single unit cell

As the imposed displacement increased, some cracks were formed and grew in different locations of the additively manufactured unit cells. Observing the specimens during the deformation showed a few locations susceptible to crack formation and propagation in different samples (Fig. 10). Despite some differences between the locations of crack formation in different samples, the trend of their load-displacement curves was similar (Fig. 11): in displacements lower than ~1.5 mm, all the samples showed elastic behavior. In the displacement ~4 mm, unit cell final fracture was observed in all the samples. The load-displacement curves (Fig. 11) were all converted to stress-strain curves in order to compare their results to the numerical and analytical results. The experimental results of the samples with the same strut thicknesses were almost similar, and the samples of each group showed relatively close stiffness and yield stress.

Fig. 12a compares the load-displacement curves obtained from experimental and simulation results for three types of single unit cell. For the experimental curve in each case, the averaged curved from three experiments (Fig. 11) was plotted. As it can be seen, there was a good correlation between the experimental and numerical results. The maximum load determined by FEM was 7%, 6%, and 20% higher than the corresponding experimental values for low, medium, and high relative density cases, respectively. The main reason for the numerical/experimental discrepancies is geometry imperfection of the 3D printed specimens and simplifying assumptions of the numerical model. Similar to experimental results, the force-displacement curves presented elastic behavior for the displacements lower than ~1.2 mm, after which strain hardening was observed, which finally led to final fracture at displacements in the range of 3–4 mm.

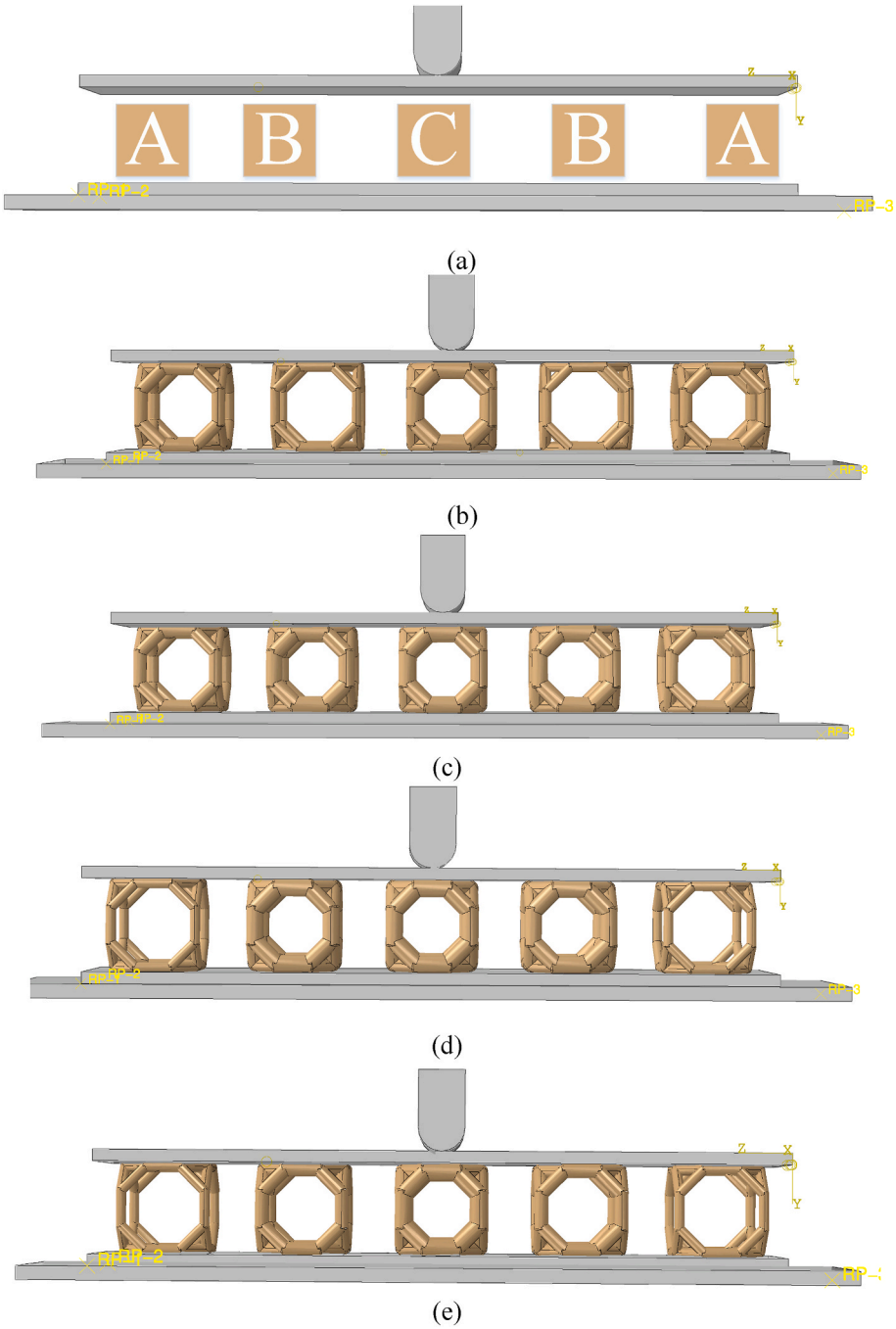

Fig. 8. (a) Definition of different positions in the sandwich panel. Different types of sandwich structures studied: (b) Type 1, (c) Type 2, (d) Type 3, and (e) Type 4.

Table 3
Different graded sandwich panel configurations examined in this study (see Fig. 8 for definition of Positions A, B, and C).

	Position A	Position B	Position C
Sandwich panel type 1	Strut radii of 3 mm	Strut radii of 2 mm	Strut radii of 4 mm
Sandwich panel type 2	Strut radii of 3 mm	Strut radii of 4 mm	Strut radii of 4 mm
Sandwich panel type 3	Strut radii of 2 mm	Strut radii of 4 mm	Strut radii of 4 mm
Sandwich panel type 4	Strut radii of 2 mm	Strut radii of 3 mm	Strut radii of 4 mm

It is worth mentioning that modeling damage is one of the strong aspects of the numerical modelling as it can predict the region of cracks very well and it can give accurate values for final fracture (see Fig. 12b, c).

Comparison between analytical, numerical, and experimental values of stiffness, Poisson's ratio, and yield stress shows excellent agreement between the numerical and analytical results, especially at small apparent densities (Fig. 13). Even at large apparent densities ($\mu = 0.5$), the difference between the numerical and analytical results was less than 7% (Figs. 13a), 20% (Fig. 13b), and 5% (Fig. 13c) for the normalized stiffness, Poisson's ratio, and normalized yield stress, respectively. The structures with square and circular cross-sections presented very close elastic properties. However, the structure with triangular cross-section had larger and smaller stiffness and Poisson's ratio, respectively with

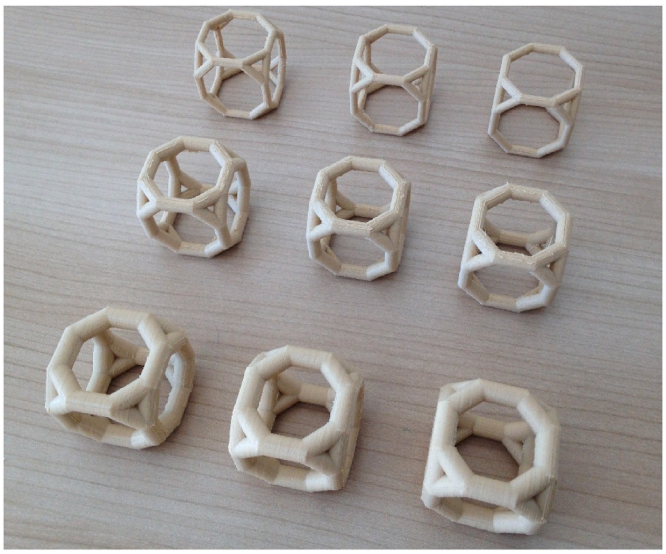

Fig. 9. The additively manufactured unit cells having equal strut length but three different thicknesses.

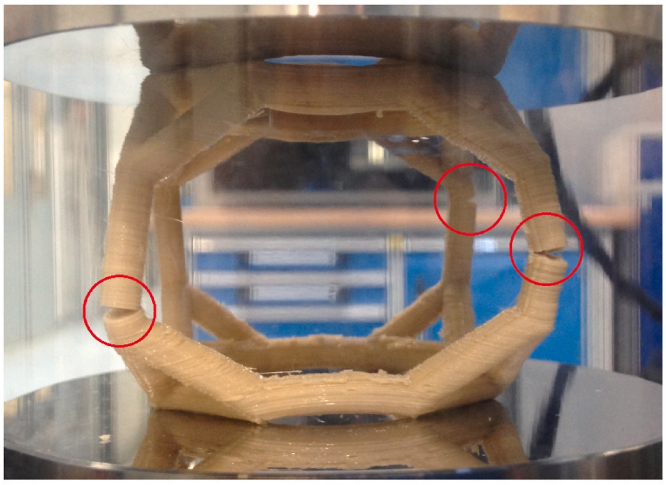

(a)

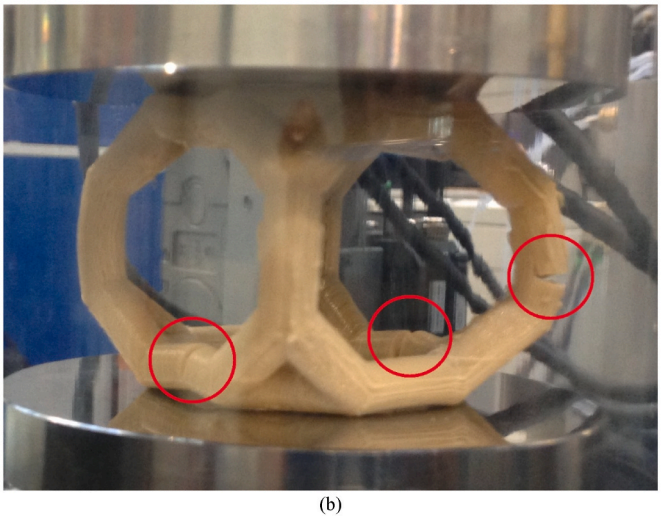

(b)

Fig. 10. Cracks formed in the struts of unit cells with (a) r/l = 0.2 and (b) r/l = 0.26 in the final stages of deformation.

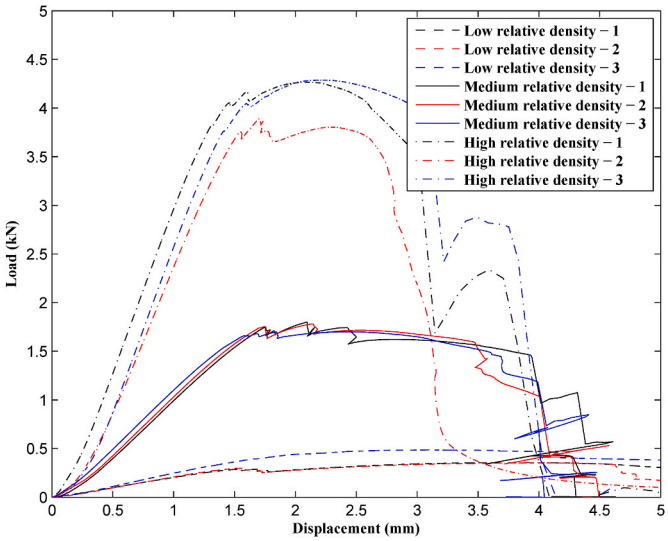

Fig. 11. Load-displacement curves for the samples with different relative densities.

respect to the corresponding values of the structures with square and circular cross-sections. This phenomenon was observed for both the analytical and numerical results. The stiffness values obtained from the experimental tests were also very close to the analytical and numerical results.

In the numerical and analytical (based on beam elements) analyses, in all the apparent densities, yielding occurred at points E and D of the inclined struts before yielding could occur in the vertical strut at the same points. On the other hand, in the experimental tests and volumetric numerical models, it was observed that failure started at the same points D and E but on the vertical strut side. This is due to the fact that in the analytical and numerical study which were both based on beam theories, the aggregation of material in the inclined struts at points B and D could not be modeled. In reality, the increase in the thickness of the inclined struts due to their overlapping at points B and D formed a wishing bone geometry that protected them against failure. If only failure in the *vertical* struts is considered (as the experimental results confirm it), the analytical, numerical, and experimental yield stress values have very good agreement (see Fig. 13c).

At the apparent density of 0.24, the normalized stiffness was 0.12 which showed a huge drop with respect to the stiffness of the solid material (Fig. 13a). However, at the same apparent density, decrease in the porous structure's yield stress with respect to that of the solid material was lower ($\left(\frac{\sigma_y}{\sigma_{ys}} \sim 0.19\right)$, see Fig. 13c.

The value of Poisson's ratio for all the cross-section types started from 0.5 for very slender struts ($\mu \rightarrow 0$) and reached ~0.25 for the apparent density of 0.5. While the numerical and analytical stiffness and Poisson's ratio values deviations from each other increased as the apparent density increased, the numerical and analytical yield stress coincided at the apparent density of 0.446 (Fig. 13c).

All the analytical relationships obtained for stiffness and Poisson's ratio of the truncated cube structure are expressed as functions of the ratio α (see Eqs. (10)–(19)). Evaluating the change in the elastic properties of truncated cube as a result of variation in α can be of interest. As the value of α increases, the ratio of the lengths of the uninclined to the lengths of the inclined struts increases, which makes the structure become more similar to a simple cube. For $\alpha = \infty$, the truncated cube becomes a cube, while for $\alpha = 0$, the structure becomes a regular octahedron.

It must be noted that by setting $\alpha = \infty$, the stiffness, Poisson's ratio, and yield stress obtained from Eqs. ((10), (12), (14), (17) and (19) become zero. This is because if the length of the inclined struts, l, is kept

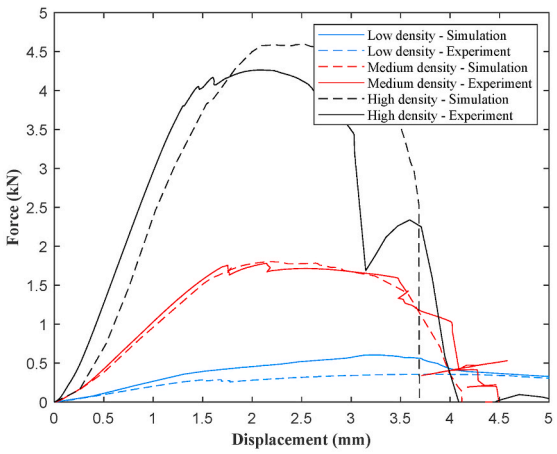

(a)

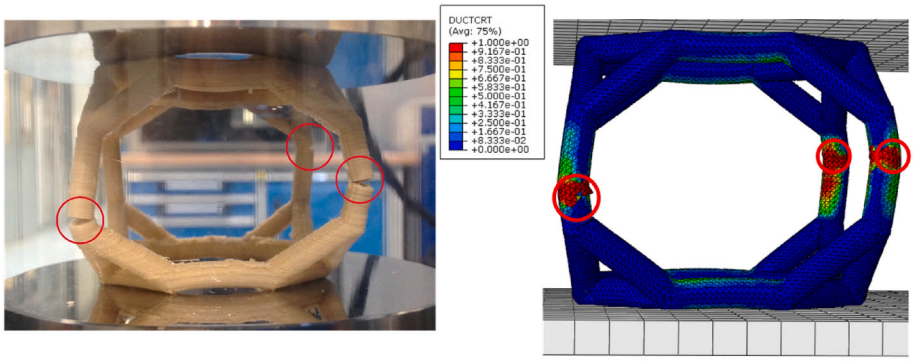

(b)

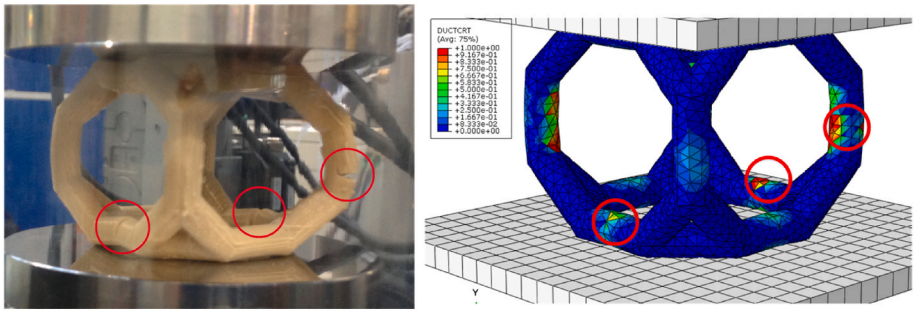

(c)

Fig. 12. Unit cells simulation results: (a) force-displacement curves for experimental and numerical model. Cracks formed in the struts of unit cells with (b) r/l = 0.2, and (c) r/l = 0.26 in the final stages of deformation for both numerical simulations and experiments.

constant, by setting $\alpha = \infty$, the dimension of each unit cell becomes infinite which yield zero relative density, stiffness, and Poisson's ratio. Since it is required to investigate the effect of α while keeping the unit cell dimension (and as a result the structure relative density) constant, the parameter $\kappa = l\left(\alpha + \sqrt{2}/2\right)$ was defined and the length of inclined struts were varied for different values of α using $l = 2\kappa/\left(2\alpha + \sqrt{2}\right)$ while keeping the unit cell dimension κ constant.

As it can be seen in Fig. 14, as the value of α is increased, the stiffness, Poisson's ratio, and yield stress increased, decreased, and increased, respectively. All the values approached asymptotic values for large α ratios. Results showed that at very large values of α, Poisson's ratio approaches zero. At $\alpha = 0$, i.e. for octahedral unit cell, the yield stress of the structure assuming that yielding occurs in the top and middle vertical struts was equal. For $\alpha > 0$, yielding always occurred in the inclined strut side of the point E and D.

All the obtained analytical elastic relationships (Eqs. (10)–(21) and (27)) are expressed as functions of the solid material's Poisson's ratio, too. Therefore, investigating its effect on the elastic properties of truncated cube structure is beneficial. It was seen that the solid material Poisson's ratio had a very small effect on the structure's normalized stiffness and Poisson's ratio, and it was almost ineffective on the truncated cube structure's yield stress (Fig. 15). Increasing the solid material Poisson's ratio from 0 to 0.5 did not change the normalized stiffness and Poisson's ratio of the truncated cube structures for more than 1.5% and 0.2%, respectively.

3.2. Sandwich panels

The loading pin was displaced until the first cubic unit cell (at the center) was completely failed. Fig. 16a–d demonstrates the final deformation of sandwich panels due to displacement of the loading pin. The

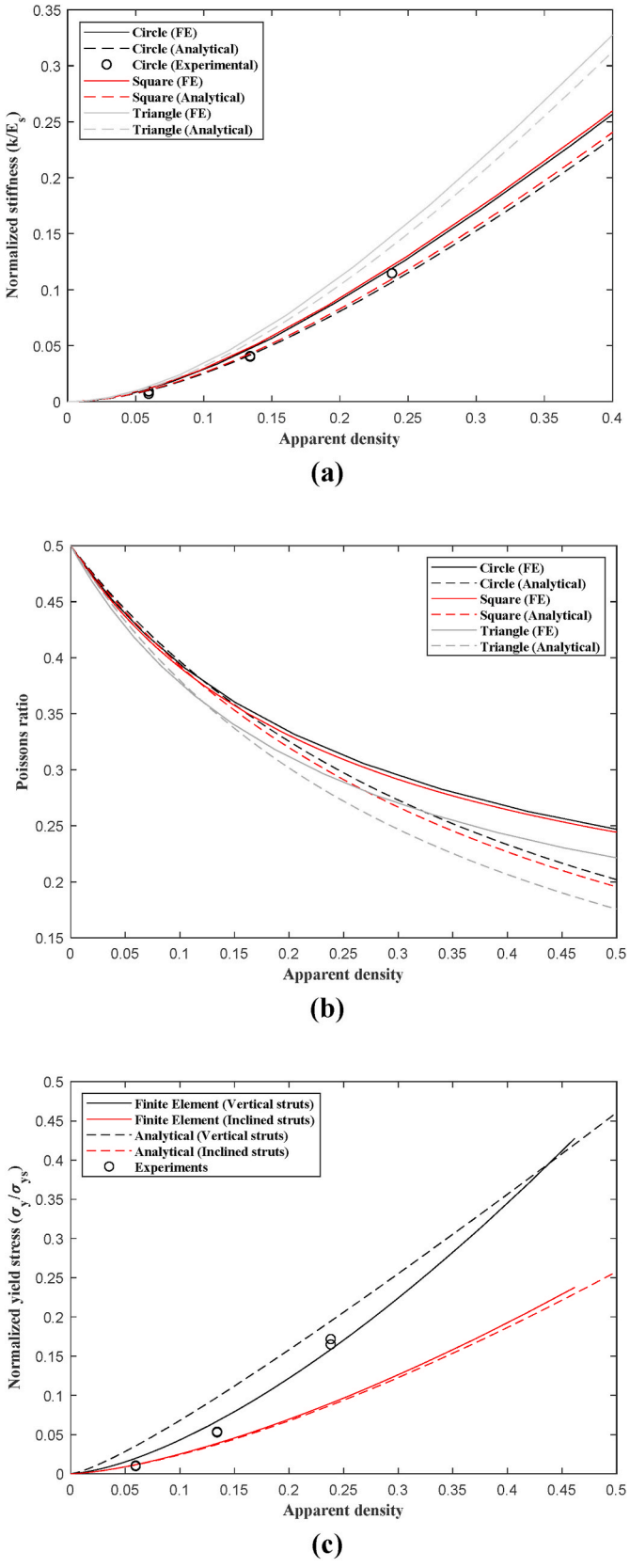

Fig. 13. Effect of apparent density on the values of (a) normalized stiffness, (b) Poisson's ratio, and (c) normalized yield stress for circular cross-section.

upper and lower aluminum plates are hidden in these figures to make it easier to observe stress counter in truncated cube unit cells. The force-displacement curves of four types of sandwich panels are presented in Fig. 17a. As indicated in this figure, the maximum displacement which is around 15 mm occurred in the case of a sandwich panel with a low-thickness unit cell (2 mm), while the minimum final displacement belonged to the sandwich panel with graded core (Type 4). The sandwich panels with high and low relative density cores presented maximum forces of 13.85 kN and 2.69 kN, respectively. The maximum load in the case of graded core was 10.4 kN, and its maximum displacement was 8.67 mm, which was the lowest final displacement among all the sandwich panels.

The force-displacement curves of all the sandwich panels have a similar trend; at low displacements (<1 mm) the force increases exponentially due to initial softening. Afterward, the vertical edges of the unit cells started buckling and failing, and the force increased at a decreasing rate. Finally, local fracture occurred in the uninclined edges, leading to a slight decrease in force recorded from the sandwich panel before the final fracture. It is worth mentioning that maximum loads are recorded at displacements around 3–6 mm in all the cases (Fig. 17a), which is the displacement range where fractures occur locally in the unit cells.

4. Discussion

4.1. Differences between experimental data and analytical/numerical results in elastic regime

Although Timoshenko beam theory was used for the numerical model, and Euler-Bernoulli beam theory was implemented for obtaining the analytical formulations the differences between numerical and analytical stiffness, Poisson's ratio, and yield stress did not exceed 7% (Figs. 13a), 20% (Fig. 13b), and 5% (Fig. 13c), respectively, even at apparent densities as large as 50%. The experimental stiffness and yield stress showed some deviations with respect to numerical/analytical results. The additively manufactured structures do not have constant cross-section areas (see Figs. 9 and 10). Layer-by-layer solidification of melted filaments creates uneven external surfaces in the manufactured specimens. Variations in the cross-section area decreases the stiffness of the structure, because in the struts with very weak portions, micro-plasticity usually starts in the very early phases of deformation, and therefore, changes the way such portions contribute in the structure's load bearing. To better model the effect of these variations in the strut cross-sections, FE solutions would be very helpful because it is possible to define elements with varying cross-section areas per each strut length. The thickness of the struts can be varied randomly along the strut using automatic randomizing functions. For such a FE study, see Ref. [19].

Since the surface roughness of the manufactured samples are almost close in the structures with all apparent densities, the larger the thickness of the strut is, the lower the effect of surface unevenness will be. This is due to the fact that by increasing the strut thickness, the ratio of area occupied by the uneven external surface of the strut to the internal area of the strut decreases. This was verified by comparing the experimental/analytical correlation in truncated cube unit cells with different strut thicknesses. As the apparent density increased, the experimental/analytical correlation improved for both the elastic modulus and yield stress values (Fig. 13).

As it can be seen in Fig. 10, the most common damaged spots in the unit cells are either the middle part of the horizontal edges or the top and bottom ends of the vertical edges. While the behaviour of horizontal edges was not studies analytically in this study (due to complexies arising from direct contact of the horizontal edges with the loading plates), the location of the latter was well predicted in both the analytical and numerical studies.

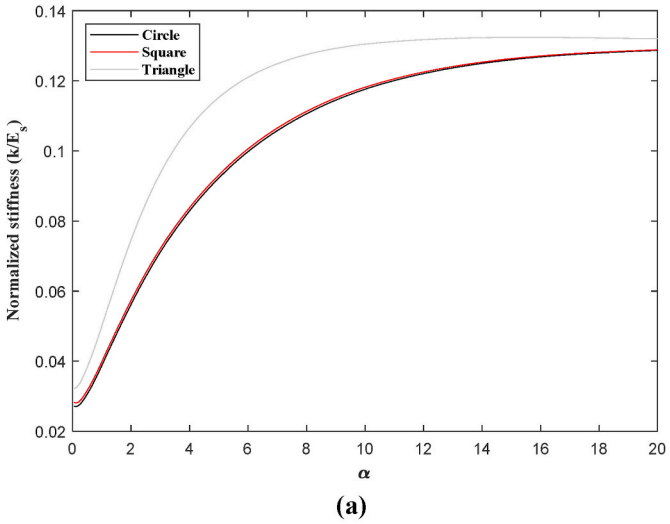

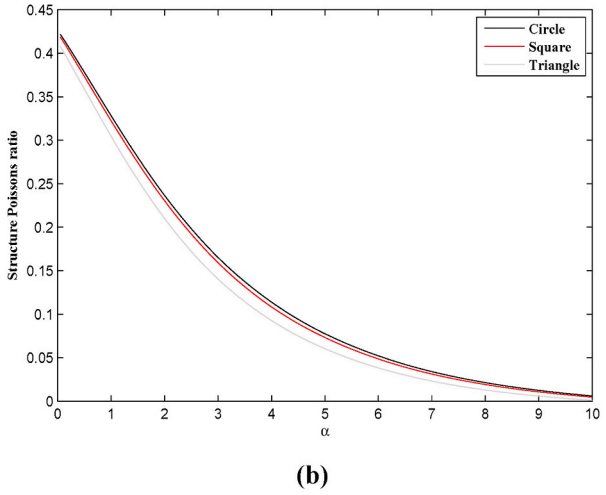

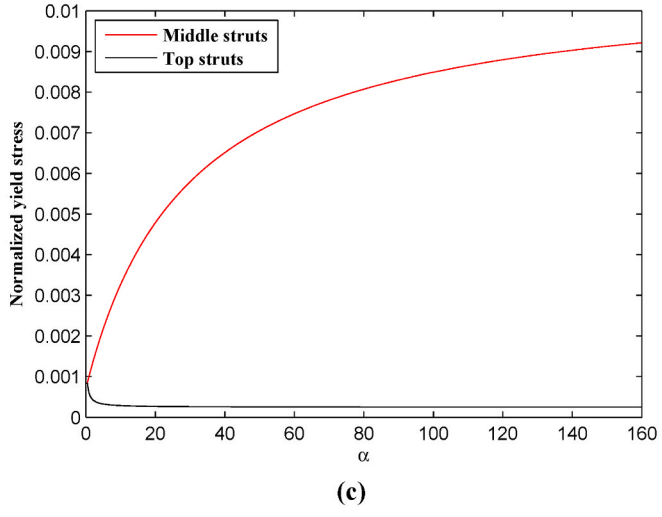

Fig. 14. Effect of length of middle vertical edge on the values of (a) normalized stiffness, (b) Poisson's ratio, and (c) normalized yield stress. The parameter $\boldsymbol{\alpha}$ is the ratio of the middle vertical edge length to the inclined edge length. The ratio $\boldsymbol{r/\kappa}$ is 0.1.

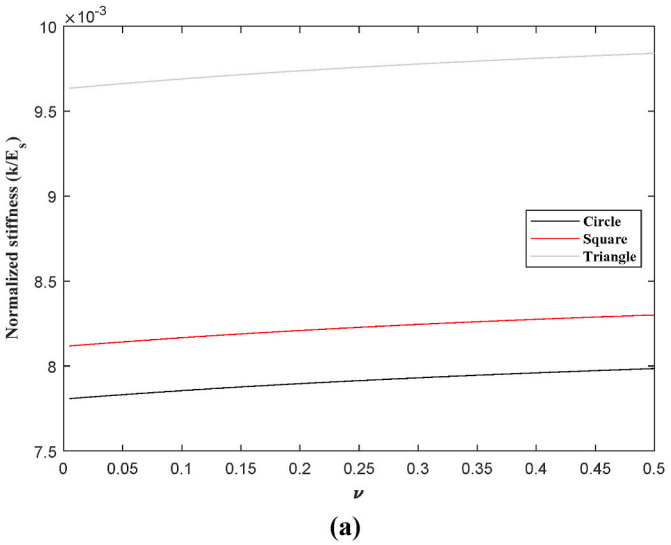

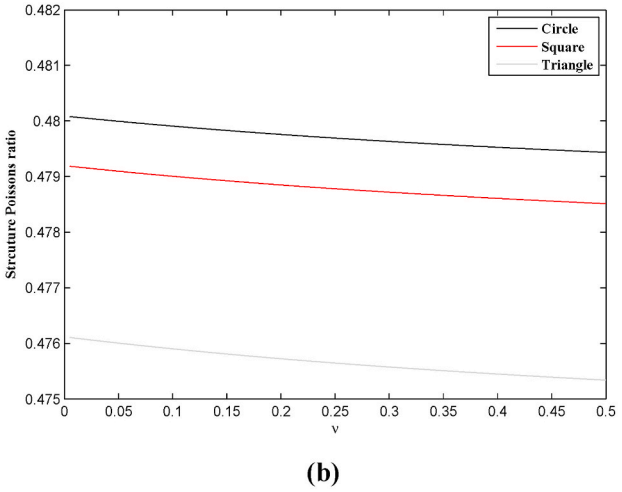

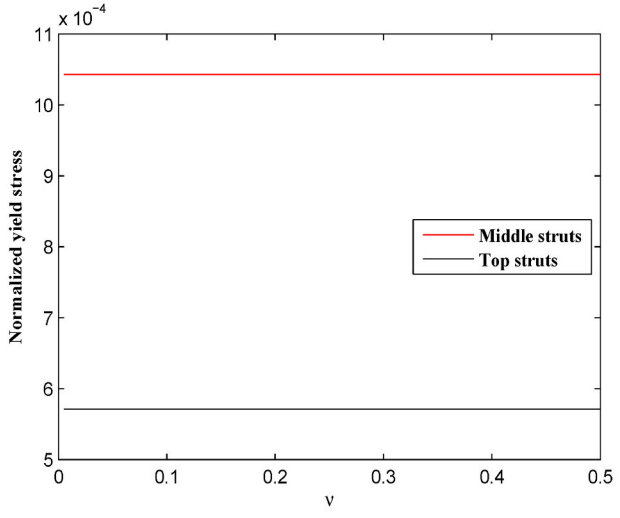

Fig. 15. Effect of the material Poisson's ratio on the values of (a) normalized stiffness, (b) Poisson's ratio, and (c) normalized yield stress.

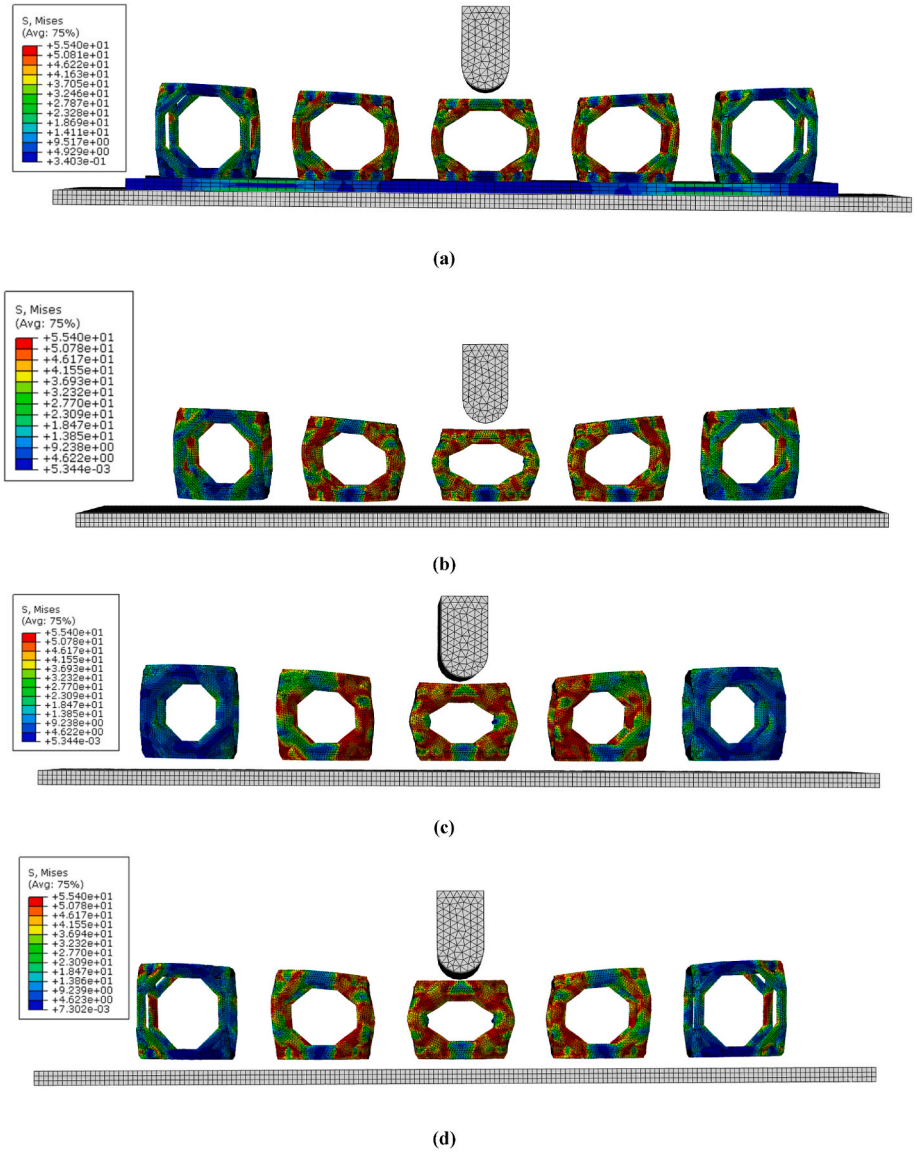

Fig. 16. The final form of deformed sandwich panels for unit cells with strut radii of (a) 2 mm, (b) 3 mm, (c) 4 mm, and (d) functionally graded cores (sample 4).

4.2. Single unit cell vs. lattice structure

One of the main contributions of the current research is obtaining analytical relationships for elastic properties of a single truncated cube unit cell. Although truncated cube unit cell has been previously presented as being a very good candidate for back-to-back lattice structures, where the boundary conditions are different from those considered in this paper, but the formulas obtained in this research for a single unit cell are also applicable to some locations of the back-to-back lattice structure where the unit cells are not completely surrounded by neighboring cells, such as implant corners, edges, etc. In most engineering applications, the exterior portions of a segment are the most susceptible locations to damage. This is also true and maybe even more serious in implants as all the external surfaces of an implant are loaded by bone tissues surrounding them. In addition to biomedical implants, a single truncated cube structure can also be useful for applications such as packaging and sandwich panels where the unit cells are not in direct contact with each other. It was shown in Fig. 14c that an equilateral truncated cube structure ($\alpha = 1$) has a yield stress at least twice of that for a simple cube structure ($\alpha = \infty$). Therefore, boxes with truncated cubic skeleton can tolerate loads at least twice the load the boxes with cubic skeleton can bear. As a result, replacing cubic boxes with truncated cubic boxes in applications such as goods transportation where a large number of boxes have to be stacked on top of each other can be beneficial. The analytical relationships obtained for truncated cube structure are very useful for obtaining fast and exact elastic mechanical properties of such structures.

Mechanical properties of a truncated cube unit cell inside a lattice structure is investigated in Ref. [41]. Comparison of yield stress between a single truncated cube unit cell, studied here, and a truncated cube unit cell inside a back-to-back lattice structure [41] can be of interest. At the apparent density of 50%, where the normalized yield stress of a single unit cell is about 0.25, the normalized yield stress of a the unit cell inside a back-to-back lattice structure is about 0.125. This can imply that at the same levels of stress, the interior parts of an implant are more susceptible to damage. This was evaluated by numerically analyzing a cubic lattice structure under compressive loading and comparing the stress level in its different locations. It was seen that the stress level in the internal parts of an implant with arbitrary macro-geometry is not essentially larger or smaller than that in its exterior parts, and depending on the loading conditions and the macro-geometry of the implant, more thorough investigations are necessary to find out which regions are the

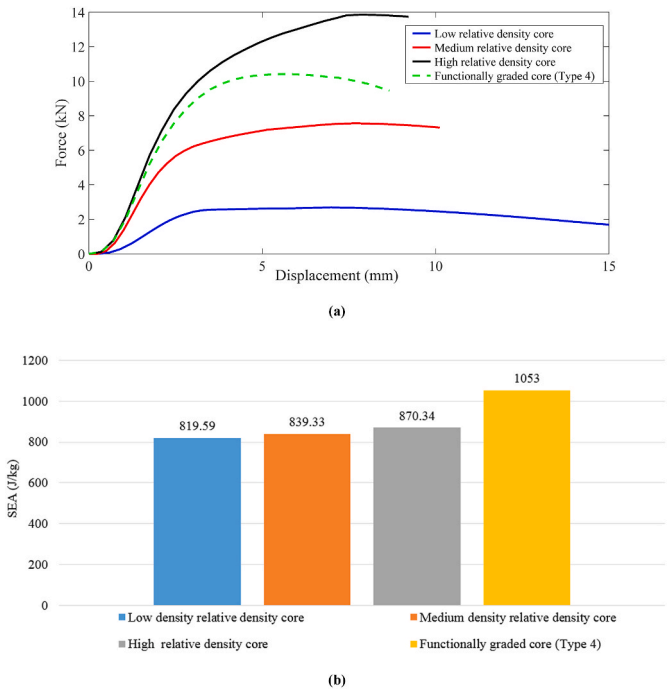

Fig. 17. Simulation results of sandwich panels: (a) force-displacement curves, (b) SEA for all types of cores.

locations where yielding first occurs.

While the Poisson's ratio of the lattice structure is about 0.2 and 0.06 for the apparent densities of 0 and 0.5, respectively, the Poisson's ratio of a single truncated cube is 0.5 and 0.25 at the same apparent densities. This huge difference between the Poisson's ratio of a single unit cell and a unit cell placed inside a lattice structure shows that the porous structure has a much higher tendency to move transversely in its exterior parts as compared to its internal regions.

4.3. Active deformation mechanisms

In single unit cell, some mechanisms such as local plasticity, buckling of the struts, interaction of neighboring struts, etc. can be influencing factors in the failure of the structure. Interaction of neighboring struts becomes active only after the structure has gone under large deformations, the start of which is marked by the densification part of a stress-strain curve which follows a plateau phase in a typical stress-strain curve of porous structures. A structure must be designed in such a way that none of its parts enter the plateau phase. Therefore, only the two failure mechanisms of local yielding and buckling must be studied to find out which of them are the first mechanism which lead to structural failure. Plotting the yield stress against the buckling stress demonstrated that the buckling stress for single truncated cube structures is several orders of magnitude larger than their yield stress for the strut radii considered.

It was shown in Fig. 15 that the effect of the material Poisson's ratios on the stiffness, yield stress and Poisson's ratio of a truncated cube structure is less than 1.5%. Therefore, simplifying the analytical relationships, Eqs. (10)–(21) and (27) by setting $\nu = 0$ or $G/E = 0.5$ does not change the results of the analytical relationships significantly.

4.4. Applications in the sandwich panels

Sandwich panels have broad applications in automobiles, marine, and aerospace industries due to their advantageous properties such as low weight and high energy absorption capacity [1]. Both energy absorption capability and mass of the sandwich structure are highly crucial in practical applications. Therefore, specific energy absorption (SEA), which is defined as energy absorption per unit mass of the structures (the mass of all the unit cells in each case), is reported in Fig. 17b.

In the present study, sandwich panels with different functionally graded core configurations were examined. The optimum design for highest energy absorption capacity was found by conducting simulations on those configurations. The highest SEAs were obtained for graded cores, where a truncated cube unit cell with strut radii of 4 mm (high relative density) was placed at the center of the sandwich panel in a symmetric manner (all the cases shown in Fig. 8 and listed in Table 3). This is due to the fact that as the roller comes into contact with the sandwich structure, the maximum stress is applied on the central unit cell (as can be seen in Fig. 16), which implies that placing a truncated cube unit cell with the highest strut radii (i.e. 4 mm) is the best possible candidate to avoid local failure. As the truncated unit cell with strut radii of 4 mm has the maximum mass, increasing the number of this cell increases the core's overall mass. SEA of structures types 1–4 was 865.22, 890.04, 910.52, and 1053 J/kg, respectively. The functionally graded sandwich panel type 4, presented the best performance while considering both energy absorption capacity and mass. The force-displacement diagram corresponding to sandwich panel type 4 is presented in Fig. 17a as the best functionality graded design. Functionally graded sandwich panels (sandwich panel type 4) increase SEA by ~21% and decrease the maximum displacement by ~2.5% with respect to the second-ranking best option (sandwich panels with high relative density core). The force-displacement curve of all the four types of graded sandwich panels are shown in Figure B1 (see Appendix B).

Moreover, the proposed functionally graded structure with the best performance (sandwich panel type 4) has a superior specific energy absorption (SEA) capability as compared to common lattice structures. For example, depending on the number of cells, this structure shows an increase in SEA by 50–100% with respect to hexagonal horseshoe and square horseshoe geometries [15]. Moreover, structures types 1–4 have higher SEAs as compared to unreinforced nylon (PA) (653 J/kg), and even short carbon fiber (SCF) reinforced PA (720 J/kg) triangular corrugated structures [55].

4.5. Easy-to-repair feature

Another special feature of using separated truncated unit cells as the core is the ability to replace the damaged unit cells with new intact ones. For the sandwich panels considered in Fig. 16, after the maximum displacement of the roller occurs, the number of damaged unit cells which require being replaced varies from 1 to 3. Therefore, there is no need to replace the whole structure, resulting in lower maintenance costs. Considering this unique feature, the functionally graded core sandwich panel (Type 4) has the optimal performance . Using separated unit cells as the core filling material provides the ability to easily change the damaged unit cells, which are not cost-effective or straightforward with common back-to-back lattice structures. Also, as discussed earlier, as compared to other unit cell types, the truncated cube structure can provide a wide range of mechanical properties which is an important parameter in desgining sandwich structures. Another unique feature of the truncated cube unit cell is that when used as the core of sandwich panels, the upper and lower face sheets can have and maintain a good contact area with the unit cell at the interface, providing high stability during deformation and hence resulting in high energy absorption capability. However, other common unit cells might not be able to maintain this stability under loading when they are positioned separated from each other.

4.6. Application in biomedical implants

If the obtained stiffness and yield stress for a single truncated cube structure are multiplied by the corresponding values of biocompatible metals (such as Ti6Al4V), it can be seen that the elastic properties of

truncated cube structures are in the range of those in a natural bone. Proximity of the elastic moduli of bones and that of the considered unit cell prevents occurrence of stress shielding in the bone surrounding the porous biomaterial. Using additive manufacturing techniques, it is possible to produce porous implants with different micro-geometrical properties at their different locations. Using the analytical relationships obtained in this paper for a single unit cell, and presented in Ref. [41] for a lattice structure, it is possible to tailor the micro-geometrical properties of the implant in its different regions to achieve a structure with arbitrary distribution of mechanical properties. For example, the struts of the exterior parts of an implant can have thicker struts to result in an implant with high strength.

5. Conclusions

In this paper, analytical solutions were derived for a single truncated cube structure with circular, square, and equilateral triangular cross-section types. Stiffness, Poisson's ratio, and yield stress of a single truncated cube structure were derived as functions of struts' cross-sectional dimensions, unit cell size, and elastic properties of the bulk material. Unit cells with three relative density levels were printed by an FDM 3D printer. The force-displacement correlation of the truncated cube unit cell under compressive loading was determined. The compressive tests were also simulated by FEM, and the results were compared with experimental results. Another significant novelty of the present research is making use of separated unit cells as the core of sandwich panels, which provide ease of repairability, and introducing a novel functionally graded core. The results show that:

- The results of analytical relationships and FEM for a single unit cell study are in good agreement in terms of the above-mentioned elastic properties (stiffness, yield stress, and Poisson's ratio).
- The experimental results of 3D printed single unit cell samples under compressive tests were also in good accordance with FEM considering damage initiation and evaluation, especially at large apparent densities. FEM was capable of determining damage initiation locations as well.
- The length of inclined and vertical struts in a truncated cube is not necessarily equal and variation of the ratio of these two lengths can alter the mechanical properties of this structure significantly. The obtained solutions in this paper are not only applicable to equilateral truncated cube unit cells, but also to truncated cube cells with arbitrary truncations.
- Results indicated that bulk material Poisson's ratio has an insignificant impact (less than 1.5%) on the relative stiffness, yield stress, and Poisson's ratio of a truncated cube structure. In this regard, simplifying the analytical relationships by setting $\nu = 0$ or $G/E = 0.5$ does not change the results of the analytical relationships significantly.
- Seven sandwich panels with identical aluminum face sheets but with different cores (three core types consisted of unit cells with uniform strut radii and four core types consisted of graded unit cells) were considered as application cases of the truncated cube unit cells. The functionally graded sandwich panel presented the best performance while considering both energy absorption capacity and mass. Functionally graded sandwich panels (Type 4) increased SEA by almost 21% and decreased the maximum displacement by 2.5% with respect to the second-ranking best option.

Authors statement

Conceptualization, R.H., A.Y. and M.B.;
Data curation, R.H. and A.Y.;
Formal analysis, R.H., A.Y. and M.B.;
Investigation, R.H., A.Y. and M.B.;
Methodology, R.H., A.Y. and M.B.;
Supervision, R.H. and M.B.;
Visualization, R.H., A.Y.;
Writing—original draft, R.H., A.Y.;
Writing—review & editing, R.H., A.Y. and M.B.
All authors have read and agreed to the published version of the manuscript.

Declaration of competing interest

The authors declare that they have no known competing financial interests or personal relationships that could have appeared to influence the work reported in this paper.

Data availability

All research data are available in the paper.

Appendix A. Supplementary data

Supplementary data to this article can be found online at https://doi.org/10.1016/j.compositesb.2022.110124.

References

[1] Safarabadi M, et al. Experimental and numerical study of buckling behavior of foam-filled honeycomb core sandwich panels considering viscoelastic effects. J Sandw Struct Mater 2020;23(8):3985–4015.
[2] Palomba G, et al. Single and double-layer honeycomb sandwich panels under impact loading. Int J Impact Eng 2018;121:77–90.
[3] Kamarian S, Bodaghi M, Song Ji. Hygrothermal effects on the buckling of soft-core sandwich plates with composite layered face sheets. Polym Compos 2020;41(10):4144–69.
[4] Le VT, Ha NS, Goo NS. Advanced sandwich structures for thermal protection systems in hypersonic vehicles: a review. Compos B Eng 2021;226:109301.
[5] Mei J, Liu J, Huang W. Three-point bending behaviors of the foam-filled CFRP X-core sandwich panel: experimental investigation and analytical modelling. Compos Struct 2022;284:115206.
[6] Torkestani A, Sadighi M, Hedayati R. Effect of material type, stacking sequence and impact location on the pedestrian head injury in collisions. Thin-Walled Struct 2015;97:130–9.
[7] Hedayati R, Ziaei-Rad S. Foam-core effect on the integrity of tailplane leading edge during bird-strike event. J Aircraft 2011;48(6):2080–9.
[8] Chen B, et al. Multifunctional cellular sandwich structures with optimised core topologies for improved mechanical properties and energy harvesting performance. Compos B Eng 2022;238:109899.
[9] Sun G, et al. On the structural parameters of honeycomb-core sandwich panels against low-velocity impact. Compos B Eng 2021;216:108881.
[10] Yang W, et al. Ballistic impact responses and failure mechanism of composite double-arrow auxetic structure. Thin-Walled Struct 2022;174:109087.
[11] Liu J, et al. Investigation on manufacturing and mechanical behavior of all-composite sandwich structure with Y-shaped cores. Compos Sci Technol 2018;159:87–102.
[12] Li H, et al. Broadband low-frequency vibration attenuation in 3D printed composite meta-lattice sandwich structures. Compos B Eng 2021;215:108772.
[13] Meng L, et al. An inverse approach to the accurate modelling of 3D-printed sandwich panels with lattice core using beams of variable cross-section. Compos Struct 2020;247:112363.
[14] Pirouzfar S, Zeinedini A. Effect of geometrical parameters on the flexural properties of sandwich structures with 3D-printed honeycomb core and E-glass/epoxy Face-sheets. In: Structures. Elsevier; 2021.
[15] Serjouei A, et al. 4D printed shape memory sandwich structures: experimental analysis and numerical modeling. Smart Mater Struct 2022;31(5):055014.
[16] Amin Yavari S, et al. Crystal structure and nanotopographical features on the surface of heat-treated and anodized porous titanium biomaterials produced using selective laser melting. Appl Surf Sci 2014;290:287–94.
[17] Heinl P, Körner C, Singer RF. Selective electron beam melting of cellular titanium: mechanical properties. Adv Eng Mater 2008;10(9):882–8.
[18] Mohammadi K, et al. Hybrid anisotropic pentamode mechanical metamaterial produced by additive manufacturing technique. Appl Phys Lett 2020;117(6):061901.
[19] Campoli G, et al. Mechanical properties of open-cell metallic biomaterials manufactured using additive manufacturing. Mater Des 2013;49:957–65.
[20] Shulmeister V, et al. A numerical study of large deformations of low-density elastomeric open-cell foams. Mech Mater 1998;30(2):125–40.
[21] Ghavidelnia N, Jedari Salami S, Hedayati R. Analytical relationships for yield stress of five mechanical meta-biomaterials. Mechanics Based Design of Structures and Machines; 2020. p. 1–23.
[22] Van der Burg M, et al. On the linear elastic properties of regular and random open-cell foam models. J Cell Plast 1997;33(1):31–54.

[23] Smith M, Guan Z, Cantwell W. Finite element modelling of the compressive response of lattice structures manufactured using the selective laser melting technique. Int J Mech Sci 2013;67:28–41.
[24] Hedayati R, et al. Improving the accuracy of analytical relationships for mechanical properties of permeable metamaterials. Appl Sci 2021;11(3):1332.
[25] Labeas G, Sunaric M. Investigation on the static response and failure process of metallic open lattice cellular structures. Strain 2010;46(2):195–204.
[26] Niendorf T, Brenne F, Schaper M. Lattice structures manufactured by SLM: on the effect of geometrical dimensions on microstructure evolution during processing. Metall Mater Trans B 2014;45(4):1181–5.
[27] Cansizoglu O, et al. Properties of Ti–6Al–4V non-stochastic lattice structures fabricated via electron beam melting. Mater Sci Eng, A 2008;492(1):468–74.
[28] Soltani A, et al. 3D printing on-water sports boards with bio-inspired core designs. Polymers 2020;12(1):250.
[29] Sun J, Yang Y, Wang D. Mechanical properties of Ti-6Al-4V octahedral porous material unit formed by selective laser melting. Adv Mech Eng 2012;2012.
[30] Ptochos E, Labeas G. Elastic modulus and Poisson's ratio determination of micro-lattice cellular structures by analytical, numerical and homogenisation methods. J Sandw Struct Mater 2012;14(5):597–626. 1099636212444285.
[31] Ptochos E, Labeas G. Shear modulus determination of cuboid metallic open-lattice cellular structures by analytical, numerical and homogenisation methods. Strain 2012;48(5):415–29.
[32] Gibson LJ, Ashby MF. Cellular solids: structure and properties. Cambridge university press; 1997.
[33] Ahmadi S, et al. Mechanical behavior of regular open-cell porous biomaterials made of diamond lattice unit cells. J Mech Behav Biomed Mater 2014;34:106–15.
[34] Babaee S, et al. Mechanical properties of open-cell rhombic dodecahedron cellular structures. Acta Mater 2012;60(6):2873–85.
[35] Hedayati R, Sadighi M. A micromechanical approach to numerical modeling of yielding of open-cell porous structures under compressive loads. J Theor Appl Mech 2016;54(3):769–81.
[36] Hedayati R, et al. Mechanics of additively manufactured porous biomaterials based on the rhombicuboctahedron unit cell. J Mech Behav Biomed Mater 2016;53:272–94.
[37] Ghavidelnia N, Bodaghi M, Hedayati R. Femur auxetic meta-implants with tuned micromotion distribution. Materials 2021;14(1):114.
[38] Hedayati R, Güven A, Van Der Zwaag S. 3D gradient auxetic soft mechanical metamaterials fabricated by additive manufacturing. Appl Phys Lett 2021;118(14):141904.
[39] Zhu H, Knott J, Mills N. Analysis of the elastic properties of open-cell foams with tetrakaidecahedral cells. J Mech Phys Solid 1997;45(3):319–43.
[40] Zadpoor AA, Hedayati R. Analytical relationships for prediction of the mechanical properties of additively manufactured porous biomaterials. J Biomed Mater Res 2016;104(12):3164–74.
[41] Hedayati R, et al. Mechanical properties of regular porous biomaterials made from truncated cube repeating unit cells: analytical solutions and computational models. Mater Sci Eng C 2016;60:163–83.
[42] Hou C. Numerical and experimental crashworthiness studies of foam-filled frusta. 2013.
[43] Mills N, et al. Finite element micromechanics model of impact compression of closed-cell polymer foams. Int J Solid Struct 2009;46(3–4):677–97.
[44] Vigliotti A, Pasini D. Stiffness and strength of tridimensional periodic lattices. Comput Methods Appl Mech Eng 2012;229:27–43.
[45] Hasan M. An improved model for FE modeling and simulation of closed cell Al-alloy foams. Adv Mater Sci Eng 2010;2010.
[46] Kim A, et al. A multi-cell FE-model for compressive behaviour analysis of heterogeneous Al-alloy foam. Model Simulat Mater Sci Eng 2006;14(6):933.
[47] Wang E, Li Q, Sun G. Computational analysis and optimization of sandwich panels with homogeneous and graded foam cores for blast resistance. Thin-Walled Struct 2020;147:106494.
[48] Sun G, et al. Low-velocity impact behaviour of sandwich panels with homogeneous and stepwise graded foam cores. Mater Des 2018;160:1117–36.
[49] Daxner T. Finite element modeling of cellular materials. In: Cellular and porous materials in structures and processes. Springer; 2010. p. 47–106.
[50] Noori H. Interlayer fracture energy of 3D-printed PLA material. Int J Adv Manuf Technol 2019;101(5):1959–65.
[51] Yousefi A, et al. Fatigue life improvement of cracked aluminum 6061-T6 plates repaired by composite patches. Materials 2021;14(6):1421.
[52] Abdel-Nasser YA. Frontal crash simulation of vehicles against lighting columns using FEM. Alex Eng J 2013;52(3):295–9.
[53] Narayana PSR, et al. Equivalent energy absorption (EEA)-A methodology for improved automotive crash & safety design. In: ASME international mechanical engineering congress and exposition. American Society of Mechanical Engineers; 2021.
[54] Documentation, A. And U. Manual, *version 6.14*. Dassault systemes; 2010.
[55] Wang B, et al. Fabrication of triangular corrugated structure using 3D printed continuous carbon fiber-reinforced thermosetting epoxy composites. Polym Test 2022;106:107469.